

The Long and the Short of It: The Benefits and Leverage of Ultraviolet-Radio Galaxy Fitting

Jessica E. Thorne,^{1*} Aaron S. G. Robotham,¹ Sabine Bellstedt,¹ Luke J. M. Davies,¹

¹ ICRAR, The University of Western Australia, 35 Stirling Highway, Crawley, WA 6009, Australia

Accepted XXX. Received YYY; in original form ZZZ

ABSTRACT

Traditionally, the far ultraviolet (FUV) to far-infrared (FIR) and radio spectral energy distributions (SEDs) of galaxies have been considered separately despite the common physical process shaping them. In this work, we explore the utility of simultaneously fitting FUV-radio SEDs using an extended version of the PROSPECT SED fitting code considering contributions from both free-free and synchrotron emission. We use a small sample of galaxies from the Deep Extragalactic Visible Legacy Survey (DEVILS) and the Key Insights on Nearby Galaxies: a Far-Infrared Survey with *Herschel* (KINGFISH) where high-quality and robust FUV-radio data are available to provide an ideal sample for testing a radio extension of PROSPECT. As the parameterisation of the radio extension links the radio continuum to the FIR emission, we explore the benefit of using radio continuum measurements as a constraint on the energy balance between dust attenuation and emission. We find that for situations where MIR-FIR photometry is unavailable, including a 1.4 GHz continuum measurement allows for improved accuracy in recovered star formation rates and dust luminosities of galaxies reducing the median uncertainty by 0.1 and 0.2 dex respectively. We also demonstrate that incorporating 3 and 10 GHz measurements allows for further constraint on the energy balance and therefore the star formation rate and dust luminosity. This demonstrates the advantage of extending FUV-FIR SED fitting techniques to radio frequencies, especially as we move into an era where FIR surveys will remain limited and radio data become abundant (i.e. with the SKA and precursors).

Key words: galaxies: evolution – galaxies: general – galaxies: star formation – galaxies: stellar content – radio continuum: galaxies

1 INTRODUCTION

Galaxy spectral energy distributions (SEDs) contain a wealth of information about the physical processes occurring within a galaxy and are shaped by contributions from stars, dust, gas, active galactic nuclei (AGN) etc (see [Walcher et al. 2011](#); [Conroy 2013](#)). Each of these components contribute at different wavelengths, leaving their imprint on a galaxy SED. As different emission mechanisms dominate in different wavelength regimes, certain wavelengths are used to measure certain astrophysical quantities of interest. For example, the stellar mass of galaxies is often measured in the optical and/or near infrared as emission from stars dominates at these wavelengths ([Zibetti et al. 2009](#); [Taylor et al. 2011](#)). In addition, star formation rates (SFRs) can be measured at ultraviolet (UV) wavelengths as this regime is dominated by short-lived OB stars ([Kennicutt & Evans 2012](#)). However, this is made difficult due to the presence of dust which preferentially absorbs shorter wavelength photons (UV-optical) and re-emits at far infrared (FIR) wavelengths ([Draine 2003](#)). To account for the impact of dust, SFRs can also be measured using the combination of UV and infrared ([Bell et al. 2005](#)), however, this measurement can be biased by dust heating from numerous low-mass stars. As there is considerable interplay between galaxy components resulting in a significant

impact on the SED, it has become more common to consider the components simultaneously (e.g. [Da Cunha et al. 2008](#); [Noll et al. 2009](#); [Robotham et al. 2020](#)).

Many codes have been developed to measure key galaxy properties by self-consistently fitting the far ultraviolet (FUV) to FIR SEDs of galaxies. Examples of these include PROSPECT ([Robotham et al. 2020](#)), MAGPHYS ([Da Cunha et al. 2008](#)), CIGALE ([Noll et al. 2009](#); [Boquien et al. 2019](#)), PROSPECTOR ([Johnson et al. 2021](#)), BEAGLE ([Chevallard & Charlot 2016](#)), and BAGPIPES ([Carnall et al. 2018](#)). Traditionally, SED fitting codes have been focused on measuring galaxy stellar masses and SFRs, however, advancements in photometric data quality have allowed for more reliable estimates of age, dust attenuation, and metallicity ([Bellstedt et al. 2020](#); [Lower et al. 2022](#); [Thorne et al. 2022b](#)).

As with the FUV-FIR SEDs of galaxies, the shape of a galaxy’s SED at radio frequencies is governed by the processes occurring within it including contributions related to star formation and the presence of an AGN. Observed radio emission can be used as a direct probe into the star-formation activity in ‘normal’ galaxies (i.e. those without AGN), as radio luminosity is known to be directly proportional to recent star-formation rate ([Condon 1992](#); [Haarsma et al. 2000](#); [Bell et al. 2003](#); [Hopkins et al. 2003](#); [Davies et al. 2017](#); [Gürkan et al. 2018](#); [Smith et al. 2021](#); [Heesen et al. 2022](#)). In addition, the shape of radio SEDs, including the spectral indices (α ,

* E-mail: jessica.thorne@icrar.org

where $S_\nu \propto \nu^\alpha$), can also be used to explore radiation laws and the cooling/heating mechanisms of the interstellar medium (ISM), and for some types of AGN can be used to probe the accretion activity and AGN timescales.

Radio SEDs of star-forming galaxies (at 1.4 GHz and higher frequencies) are generally the result of the combination of two distinct mechanisms, free-free emission and absorption, and synchrotron emission. These emission mechanisms arise from different physical processes in the galaxy. As such, in order to robustly link the observed radio emission to a physical process, and therefore a star formation or AGN mechanism, they must first be deconstructed into their respective components.

Synchrotron emission, the emission of photons from charged particles (usually electrons) spiraling around magnetic field lines at close to the speed of light, dominates the radio emission from most normal galaxies at frequencies below $\nu \sim 30$ GHz. Synchrotron emission in star-forming galaxies is thought to be produced by supernova remnants which accelerate electrons to relativistic speeds (Harwit & Pacini 1975). The supernova rate of galaxies is inherently linked to the birth of high-mass stars, as only stars more massive than $\sim 8M_\odot$ can produce the Type II and Type Ib core-collapse supernovae whose remnants are thought to accelerate most of the electrons in normal galaxies (Condon 1992). This means that the non-thermal radio luminosity provides a measure of the current star formation on timescales of ~ 100 Myr for an assumed supernova rate and IMF (Condon et al. 2002).

Thermal free-free emission is powered by the ionisation of H II regions by UV flux from the same high-mass stars that eventually produce the supernovae remnants associated with non-thermal synchrotron emission (but at an earlier stage in their lifecycle). This means that, unlike synchrotron, free-free emission is a direct, near-instantaneous tracer of star formation. Despite this, free-free emission is rarely used as a radio-continuum SFR indicator as at the low frequencies typically targeted by large radio surveys, the radio continuum is overwhelmingly dominated by synchrotron emission. Isolating the free-free contribution requires either model fitting using well-sampled radio-continuum SEDs (Price & Duric 1992; Tabatabaei et al. 2017) or high-frequency observations ($\nu > 20$ GHz) where the contribution from synchrotron emission is much lower (Murphy et al. 2012).

One of the challenges with studying the SEDs of galaxies at radio frequencies is that most surveys target a single radio frequency or band (mostly 1.4 GHz) and differences in sensitivity, resolution, and data processing techniques prohibit coherent radio SED analysis of many galaxies (Tabatabaei et al. 2017). In the coming decades, the Square Kilometer Array (SKA) and its pathfinder projects will significantly increase the amount of radio data available for galaxies with robust multiwavelength imaging at improved resolution and sensitivity. However, many of the SKA and pathfinder surveys (Meyer 2009; Norris et al. 2011; Jarvis et al. 2016; Koribalski et al. 2020; McConnell et al. 2020; Shimwell et al. 2022; de Gasperin et al. 2023) will still be focused on a single radio band and multiple surveys will have to be combined to study radio SEDs at multiple frequencies.

To make the most of this wealth of new radio data, unpacking the relative contributions of free-free and synchrotron emission in different galaxy types will be vital. This cannot be done using one or two data points alone and ideally requires measurements at as many different radio frequencies as possible.

An alternative to requiring many different radio measurements is to simultaneously consider the FUV-FIR and radio regimes. As discussed previously, radio emission, both free-free and synchrotron, is inherently linked to star formation activity as is the shape of galaxy

SEDs at FUV-NIR and FIR wavelengths through both the slope of the FUV-NIR regime and the re-emission by dust at FIR wavelengths. This means that the FUV-FIR SEDs of galaxies can be used to help constrain the normalisation of the free-free and synchrotron radio continuum and aid in their separation.

Although it is theoretically straightforward to couple the observed radio emission to the star-formation rate or FIR luminosity derived from SED fitting, this has only previously been implemented in the SED-fitting codes CIGALE (Noll et al. 2009; Boquien et al. 2019) and MAGPHYS (da Cunha et al. 2015). However, the CIGALE implementation (Dey et al. 2022) uses only a single power-law component to model the radio continuum despite the known differences in spectral indices between the free-free and synchrotron components. Drouart et al. (2021) and Seymour et al. (2022) also simultaneously fit the FUV-radio SED of a high redshift radio galaxy using a bespoke tool to fit PÉGASE templates (Fioc & Rocca-Volmerange 2019) for the FUV-FIR in combination with an analytical function at radio frequencies. As with the CIGALE implementation, the analytic function used by Drouart et al. (2021) and Seymour et al. (2022) does not separate the contributions from free-free and synchrotron emission. Using a sample of low-redshift galaxies, Tabatabaei et al. (2017) demonstrated that spectral indices derived using a single power-law component can differ significantly from the synchrotron spectral indices derived using a two-component model. Hence, the CIGALE and Drouart et al. (2021) implementations are limited in their ability to provide a robust physical interpretation of the observed radio emission. The assumption of a single power-law component also prevents the estimation of the relative contributions from the free-free and synchrotron components. The radio extension of MAGPHYS described in da Cunha et al. (2015) separates the radio emission into free-free and synchrotron contributions but uses fixed spectral indices for both components and a fixed free-free contribution of 10 per cent at 20cm. However, this implementation is applied to a sample of galaxies with a single radio measurement at 1.4 GHz and therefore a sophisticated decomposition of the radio spectrum would be unnecessary.

In this work, we extend the PROSPECT FUV-FIR SED-fitting code to radio frequencies considering both the contribution from free-free and synchrotron processes. We apply the extended PROSPECT code to a small sample of galaxies to demonstrate the utility in simultaneously fitting FUV-radio SEDs and highlight its viability to be applied to much larger samples that will be available in the SKA era. This work is structured as follows. Section 2 describes the additional data sets used to supplement the DEVILS data. We describe the radio extension to PROSPECT and its implementation in Section 3. The resulting radio SED parameters and their correlation with other galaxy properties are explored in Section 4 and the 1.4 GHz Luminosity – SFR relation for the sample is presented in Section 5. In Section 6 we explore the use of radio continuum data in providing constraint on dust emission in instances where FIR data is not available. We summarise our results in Section 7. Throughout this work, we use a Chabrier (2003) IMF and all magnitudes are quoted in the AB system. We adopt the Planck Collaboration et al. (2016) cosmology with $H_0 = 67.8 \text{ km s}^{-1} \text{ Mpc}^{-1}$, $\Omega_M = 0.308$ and $\Omega_\Lambda = 0.692$.

2 DATA

2.1 Deep Extragalactic Visible Legacy Survey

For this work, we use the Deep Extragalactic Visible Legacy Survey (DEVILS; Davies et al. 2018). DEVILS is an optical spectroscopic redshift survey using the Anglo-Australian Telescope specifically

designed to have high spectroscopic completeness over a large redshift range ($z < 1$) in three well-studied extragalactic fields: XMM-LSS/D02, ECFDS/D03, and COSMOS/D10 covering a total of 4.5 deg². As per Thorne et al. (2021, 2022a,b), we use the spectroscopic and photometric data from the D10-COSMOS field as it is the deepest field. We use the DEVILS photometry catalogue derived using the PROFOUND source extraction code (Robotham et al. 2018) and described in depth by Davies et al. (2021). PROFOUND is used for source finding and photometry extraction consistently across 22 bands spanning the FUV-FIR (1500 Å–500 μm) and includes GALEX *FUVNUV* (Zamojski et al. 2007), CFHT *u* (Capak et al. 2007), Subaru HSC *griz* (Aihara et al. 2019), VISTA *JHK_s* (McCracken et al. 2012), Spitzer *IRAC1 IRAC2 IRAC3 IRAC4 MIPS24 MIPS70* (Laigle et al. 2016; Sanders et al. 2007), and Herschel *P100 P160 S250 S350 S500* (Lutz et al. 2011; Oliver et al. 2012) bands. The DEVILS redshift catalogues spanning $0 < z < 8$ have been compiled using photometric, grism, and spectroscopic redshifts and are described in Thorne et al. (2021).

To extend the FUV-FIR DEVILS photometry to longer wavelengths we use data from the MeerKAT International Gigahertz Tiered Extragalactic Explorations (MIGHTEE; Jarvis et al. 2016) and COSMOS-XS (Algera et al. 2020; van der Vlugt et al. 2021) surveys to select a sample of galaxies with high quality FUV-radio data. The COSMOS field is also covered by larger area surveys such as the VLA-COSMOS 3 GHz Large Project (Smolčić et al. 2017) and the VLA-COSMOS 1.4 GHz Deep Project (Schinnerer et al. 2007) however the 3 GHz survey has significantly finer resolution (0.75 arcseconds) than the other surveys and is known to resolve out flux for extended sources. Additionally, the COSMOS 1.4 GHz Deep Project has been superseded by MIGHTEE.

2.1.1 MeerKAT International Gigahertz Tiered Extragalactic Explorations (MIGHTEE)

The MIGHTEE large survey project will survey four well-studied deep extragalactic fields, totaling 20 deg² to μJy sensitivity at GHz frequencies using the MeerKAT telescope (Jarvis et al. 2016). MIGHTEE uses simultaneous continuum (Heywood et al. 2022), polarimetry (Sekhar et al. in prep.), and spectral line (Maddox et al. 2021) measurements with MeerKAT’s L-band (870–1670 MHz) receivers.

In this work, we make use of the Level-1 ‘Early Science’ continuum catalogue for the COSMOS field presented in Heywood et al. (2022) centered at 1.284 GHz. This consists of a single pointing in the COSMOS field, observed for 25 hours for an on-source time of 17.45 hours. MIGHTEE continuum data are imaged twice, with a Briggs’ robust parameter of 0.0 and -1.2, resulting in a higher sensitivity image as well as a finer angular resolution image. The COSMOS pointing reaches a thermal noise (measured away from the main lobe of the primary beam) of 1.9 μJy beam⁻¹ in the robust 0.0 image, with an angular resolution of 8.6 arcsec. The robust -1.2 image reaches 6 μJy beam⁻¹ with an angular resolution of 5 arcsec. Source finding was completed using PYBDSF (Mohan & Rafferty 2015) to locate and characterise components.

We also make use of the source classifications from Whittam et al. (2022) to identify radio-loud AGN in the MIGHTEE sample. RLAGN were selected using the infrared–radio correlation (IRRC) to identify sources with significantly more radio emission than would be expected from star-formation alone. The IRRC can be quantified

by the parameter q_{IR} which is defined as follows:

$$q_{\text{IR}} = \log_{10} \frac{L_{\text{IR}}(W)/3.75 \times 10^{12} \text{Hz}}{L_{1.4 \text{GHz}}(W \text{Hz}^{-1})}, \quad (1)$$

where L_{IR} is the total infrared luminosity between 8–1000 μm. This is divided by the central frequency of 3.75 × 10¹² Hz (80 μm) so that q_{IR} is a dimensionless quantity. They use the stellar mass and redshift dependent IRRC from Delvecchio et al. (2021) and select sources which lie more than 0.43 dex below the best fit correlation as having a radio excess (this corresponds to 2σ, where σ is the intrinsic scatter in the relation). 301 MIGHTEE sources were not classified as radio loud as they did not have reliable constraints on the total infrared luminosity, however, none of these objects are in our final sample.

2.1.2 COSMOS-XS

The COSMOS-XS survey (Algera et al. 2020; van der Vlugt et al. 2021) combines two single VLA pointings at sub-microJansky depth in the COSMOS field at X-band (10 GHz, 90 hours) and S-band (3 GHz, 100 hours). The X band covers a bandwidth of 4096 MHz centered at 10 GHz while the S band covers a bandwidth of 2048 MHz centered at 3 GHz.

Imaging of both data sets was performed using the standalone imager WSCLEAN (Offringa et al. 2014), incorporating *w*-stacking to account for the non-coplanarity of the baselines. Both images were created via Briggs weighting, with a robust parameter of 0.5. The images at both frequencies have a resolution of ~2″, which is large enough to avoid resolving out faint sources. The area overlap between the two frequency images covers approximately 30 arcmin², all of which lies within the DEVILS D10 field and MIGHTEE coverage.

2.1.3 Sample Selection

To generate a combined catalogue spanning the FUV-radio regimes, we position match the MIGHTEE catalogue to our catalogue with a 2″ radius using the `coordmatch` function from the R `CELESTIAL` package¹ and find radio counterparts for 6,845 of our sources. We visually inspect the optical and radio source positions to ensure that we are matching the radio object to the correct optical object. We then position match the COSMOS-XS sources to this combined catalogue again using a 2″ radius. This results in a sample of 52 DEVILS galaxies with measurements at 1.4, 3, and 10 GHz.

To ensure all sources have secure redshifts we limit our sample to only objects with spectroscopic redshifts in the DEVILS-D10 catalogue. As the radio extension implemented in PROSPECT (described below) uses FIR emission to predict the free-free emission at 1.4 GHz we also want to ensure that our FIR emission is well constrained. To do this we limit our sample to only objects with a flux density measurement above 3.63 × 10⁻⁵ Jy (20th mag) in at least one FIR band.

These implemented cuts result in a sample of 33 galaxies with spectroscopic redshifts and high-quality FUV-radio photometry.

2.2 KINGFISHER

To supplement our higher redshift DEVILS galaxies with systems in the local Universe, we use the union of the KINGFISH (Key Insights on Nearby Galaxies: A Far-Infrared Survey with *Herschel*;

¹ <https://github.com/asgr/celestial>

Table 1. The parameters used by ProSPECT in this work. We list the parameter name, a brief description, whether it is fit in linear or logarithmic (log) space or if it is fixed, the range of allowed values and any imposed non-uniform prior.

Parameter	Description	Type	Units	Values	Prior
mSFR	peak star formation rate	log	$M_{\odot} \text{ yr}^{-1}$	[-3,4]	
mpeak	lookback time when peak star formation occurred	linear	Gyr	[-2,13.38]	
mperiod	width of the SFH	log	Gyr	$[\log_{10}(0.3),2]$	$100 \text{ erf}(m\text{period} + 2) - 100$
mskew	skewness of the SFH	linear		[-0.5,1]	
Zfinal	final gas-phase metallicity	log		[-4, -1.3]	
alpha_SF_birth	Power law of the radiation field heating birth cloud dust	linear		[0,4]	$\exp(-\frac{1}{2}(\frac{\alpha_{\text{birth}}+2}{1})^2)$
alpha_SF_screen	Power law of the radiation field heating general ISM dust	linear		[0,4]	$\exp(-\frac{1}{2}(\frac{\alpha_{\text{screen}}+2}{1})^2)$
tau_birth	optical depth of the birth clouds	log		[-2.5,1]	$\exp(-\frac{1}{2}(\frac{\tau_{\text{birth}}-0.2}{0.5})^2)$
tau_screen	optical depth of the general ISM	log		[-5,1]	$-20 \text{ erf}(\tau_{\text{screen}} - 2)$
AGNan	angle of observation	linear	deg	[0.001,89.990]	
AGNlum	bolometric luminosity of AGN source	log	erg s^{-1}	[35,49]	
AGNta	optical depth tau	log		[-1,1]	
AGNrm	outer to inner torus radius ratio	fixed		60	
AGNbe	beta dust parameter	fixed		-0.5	
AGNal	gamma dust parameter	fixed		4.0	
AGNct	opening angle of torus	fixed	deg	100	
ff_frac_SF	fraction of free-free radio emission contribution at 1.4 GHz	log		[-5,-0.5]	
sy_power_SF	spectral index of the synchrotron radio emission	linear		[-2.2,0]	
ff_power_SF	spectral index of the free-free radio emission	fixed		-0.1	

Kennicutt et al. 2011; Dale et al. 2012) and SINGS (*Spitzer* Infrared Nearby Galaxies Survey, Kennicutt et al. 2003; Dale et al. 2005, 2007) samples. The galaxies in the KINGFISH sample were selected to cover a wide range of galaxy properties and ISM conditions found in the nearby Universe to better understand the physical processes linking star formation and the ISM.

SINGS recovered infrared imaging and spectroscopy for 75 nearby galaxies spanning a broad range of galaxy properties and star formation environments, while KINGFISH provided far-infrared/submillimeter data for a sample of 61 nearby galaxies, of which 57 are also SINGS targets. Recently, Dale et al. (2017) published updated global photometry for the 79 galaxies that comprise the union of the KINGFISH and SINGS samples, with photometry spanning the FUV to submillimeter. We use all available FUV-NIR photometry, namely *GALEX* FUV & NUV (Gil de Paz et al. 2007), Harris *B,V,R,I* (Dale et al. 2007), SDSS *u,g,r,i,z* (Alam et al. 2015), 2MASS *J,H,Ks* (Jarrett et al. 2003), *Spitzer* IRAC Channels 1-4, WISE bands 1-4 (Wright et al. 2010; Jarrett et al. 2013), *Spitzer* MIPS 24,70 and 160 μm , *Herschel* PACS 70,100, and 160 μm , *Herschel* SPIRE 250, 350, and 500 μm (Dale et al. 2012) and include 850 μm measurements from James Clerk Maxwell Telescope (JCMT, Holland et al. 1999) SCUBA or *Planck* High-Frequency Instrument (HIFI, Planck Collaboration et al. 2016) where available. The photometry provided by Dale et al. (2017) do not include corrections for galactic dust extinction, so we correct for this using the $E(B-V)$ values provided and the $R(V)$ dependent curve presented in Fitzpatrick (1999)².

To extend these FUV-FIR SEDs to radio frequencies we use the measurements presented in Tabatabaei et al. (2017) spanning 1.36 – 10 GHz. From the 61 galaxies in the KINGFISH sample, 50 galaxies with declinations ≥ -21 deg were selected and formed the KINGFISHER (KINGFISH galaxies Emitting in Radio) sample. For this sample, most radio measurements were made using

the Effelsberg 100-m radio telescope, however, these data are supplemented with measurements using the Very Large Array (VLA), Westerbork Synthesis Radio Telescope, and Green Bank Telescope (see Tabatabaei et al. 2017 for more details). Most galaxies have measurements at 10.7, 4.8, and 1.36-1.4 GHz however some galaxies have not been observed at all three frequencies. Additional data has been included at 8.4, 5, and 2.7 GHz where available. The flux densities provided by Tabatabaei et al. (2017) were integrated up to the optical radius in order to be consistent with measurements in the IR.

2.2.1 Sample Selection

To ensure good constraint on the normalisation and shape of the SED at radio frequencies we remove upper limits and restrict our analysis of the KINGFISHER sample to just galaxies with at least three radio data points. To ensure that we are using the correct bandpass we also do not use data points where the telescope or band used for a measurement is not explicitly stated in the sample catalogues or papers. Finally, we also remove galaxies with an $E(B-V) > 0.1$ to ensure that the galactic dust extinction corrections do not bias our results. These cuts result in a sample of 34 galaxies.

3 METHODS

To fit the FUV-radio SEDs, we extend the SED fitting technique described in Thorne et al. (2022a) to also include a flexible radio extension. We briefly outline the ProSPECT implementation from Thorne et al. (2022a) and then describe the extension to radio frequencies.

3.1 ProSPECT

We use the ProSPECT SED fitting code (Robotham et al. 2020), with the Bruzual & Charlot (2003) stellar templates, Chabrier (2003)

² This is done using the `DUST_EXTINCTION` python package (https://github.com/karllark/dust_extinction)

IMF and the Charlot & Fall (2000) dust attenuation and Dale et al. (2014) dust re-emission models. In our analysis, we use the `massfunc_snorm_trunc` parameterisation for the star formation history, which takes the form of a skewed Normal distribution, with the peak position (`mpeak`), peak SFR (`mSFR`), SFH width (`mperiod`), and SFH skewness (`mskew`) set as free parameters. The SFH is anchored to 0 at a lookback time of 13.4 Gyr, selected to be the age at which galaxies start forming (equivalent to $z = 11$, Oesch et al. 2016).

In addition to the five free parameters specifying the star formation and metallicity histories, we include four free parameters to describe the contribution of dust to the SED. Within `PROSPECT` the dust is assumed to exist in two forms; in birth clouds formed around young stars ($\text{age} < 10^7$ yr), or distributed as a screen in the ISM. For each of these components, we include two free parameters, describing the dust opacity (`tau_screen`, `tau_birch`), and the dust radiation field intensity (`alpha_screen`, `alpha_birch`). Figure 3 of Thorne et al. (2021) shows the impact of each parameter on a generated galaxy SED.

We also include an AGN component by incorporating the model outlined in Fritz et al. (2006) and Feltre et al. (2012). This models the primary source as a composition of power-laws, with different spectral indices as a function of the wavelength. To model the contribution from the torus, the Fritz et al. (2006) model uses a simple but realistic torus geometry, a flared disc, and a dust grain distribution function including a full range of grain sizes and assumes that the dust in the AGN torus is smoothly distributed. Within `PROSPECT` we model the AGN contribution by fitting the luminosity of the central source (`AGNlum`), optical depth at $9.7\mu\text{m}$ (`AGNta`), and angle of observation (`AGNan`). We also re-attenuate the emission from the central source and dust torus through the general ISM screen (see figure 1 of Robotham et al. 2020).

3.2 Radio Extension

`PROSPECT` models the emission of a galaxy in radio frequencies using a mixture of free-free (thermal) and synchrotron (non-thermal) radio emission using a prescription based on the work of Marvil et al. (2015).

Essentially, the radio continuum is computed by combining the relations from Kennicutt (1998)³ and Murphy et al. (2011) to obtain a relation for the optically thin free-free radio flux density, $S_{\text{ff}}(\nu)$:

$$S_{\text{ff}}(\nu) = 1.4 \times 10^{10} \left(\frac{FIR}{\text{W m}^{-2}} \right) \times \left(\frac{T_e}{10^4 \text{ K}} \right)^{0.45} \times \left(\frac{\nu}{\text{GHz}} \right)^{\alpha_{\text{ff}}}, \quad (2)$$

which, assuming $\alpha_{\text{ff}} = -0.1$, gives a normalisation at 1.4 GHz of

$$S_{\text{ff}}(1.4 \text{ GHz}) = 13536775000 \left(\frac{FIR}{\text{W m}^{-2}} \right) \times \left(\frac{T_e}{10^4 \text{ K}} \right)^{0.45} \quad (3)$$

This can therefore be used to define the free-free contribution to the radio continuum as a function of frequency:

$$S_{\text{ff}}(\nu) = S_{\text{ff}}(1.4 \text{ GHz}) \times \left(\frac{\nu}{1.4 \text{ GHz}} \right)^{\alpha_{\text{ff}}}. \quad (4)$$

In each case, we assume an electron temperature (T_e) of 10^4 K as

per Marvil et al. (2015) and a free-free spectral index (α_{ff}) of -0.1. The `FIR` parameter is used as an estimate of the FIR flux density between 42.5 and $122.5 \mu\text{m}$ and is calculated in Marvil et al. (2015) by combining the 60 and $100 \mu\text{m}$ flux densities into a single value. Within `PROSPECT` we instead use the Dale et al. (2014) dust emission model fits to calculate the total FIR emission associated with star formation.

The contribution to the radio from synchrotron emission is then calculated using the free-free fraction (f_{ff}) and synchrotron spectral index (α_{sy}) parameters:

$$S_{\text{sy}}(\nu) = \left(S_{\text{ff}}(1.4 \text{ GHz}) \times \frac{1 - f_{\text{ff}}}{f_{\text{ff}}} \right) \times \left(\frac{\nu}{1.4 \text{ GHz}} \right)^{\alpha_{\text{sy}}} \quad (5)$$

The total radio continuum flux density is then:

$$S_{\text{tot}}(\nu) = S_{\text{ff}}(\nu) + S_{\text{sy}}(\nu) \quad (6)$$

For this work, we only consider radio emission associated with star formation (using `addradio_SF`) as although some of our galaxies are expected to have radio emission produced by an AGN, this additional emission can be modelled by the synchrotron component. In these cases, the free-free fraction will be lower than expected from purely star formation and any changes to the slope of the radio continuum can be captured by the free synchrotron spectral index parameter. Radio emission associated with an AGN component can also be added in `PROSPECT` using `addradio_AGN` where the `FIR` parameter is calculated using only the AGN component's contribution to the FIR emission. However, modelling the radio continuum using four distinct power-law components would result in degenerate solutions unless significantly more data over a larger frequency range are used.

In addition to the free parameters described above, we allow the free-free fraction (`ff_frac_SF`) and synchrotron spectral index (`sy_power_SF`) parameters to vary freely but fix the free-free spectral index, `ff_power_SF` = -0.1. The spectral index of the synchrotron radio emission is typically between -0.8 and -0.6 for synchrotron emission generated from star-formation Condon (1992), however, when fitting, we allow it to vary freely between -2.2 and 0. This allows for where the shape of the radio SED is flatter due to contributions from radio-loud AGN (this is also the range used by Tabatabaei et al. 2017). The fraction of free-free HII nebular plasma free-free radio emission at 1.4 GHz is modelled within `PROSPECT` using the `ff_frac_SF` parameter. Condon & Yin (1990) suggest that the free-free fraction is typically seen to span the range 0.05 to 0.2 for star-forming galaxies. Again, because some galaxies might have radio contributions from an AGN, we fit using a range of $\log_{10}(\text{ff_frac_SF}) = [-5, -0.5]$, where a lower value corresponds to less free-free emission, and more contribution from synchrotron emission either from star-formation or an AGN. Both radio parameters are fit simultaneously with the usual 12 parameters relating to the star formation and metallicity histories, and the dust and AGN components.

Table 1 lists all the parameters used in this work, a brief description, whether they are fit in linear or logarithmic space or are fixed, and the allowed values.

We implement `PROSPECT` in a Bayesian manner using a combination of genetic optimisation and Markov Chain Monte Carlo (MCMC) phases using the `HIGHLANDER R` package⁴. `HIGHLANDER` alternates between genetic optimization using the `CMAESHPC`⁵ and an

³ The derivation of this relation makes a number of assumptions including a Salpeter (1955) IMF, solar abundances and that dust re-radiates all of the bolometric luminosity. Changes to the metallicity and IMF will therefore change the predicted free-free radio flux density however this is expected to only be a minor difference.

⁴ <https://github.com/asgr/Highlander>

⁵ <https://github.com/asgr/cmaeshpc>

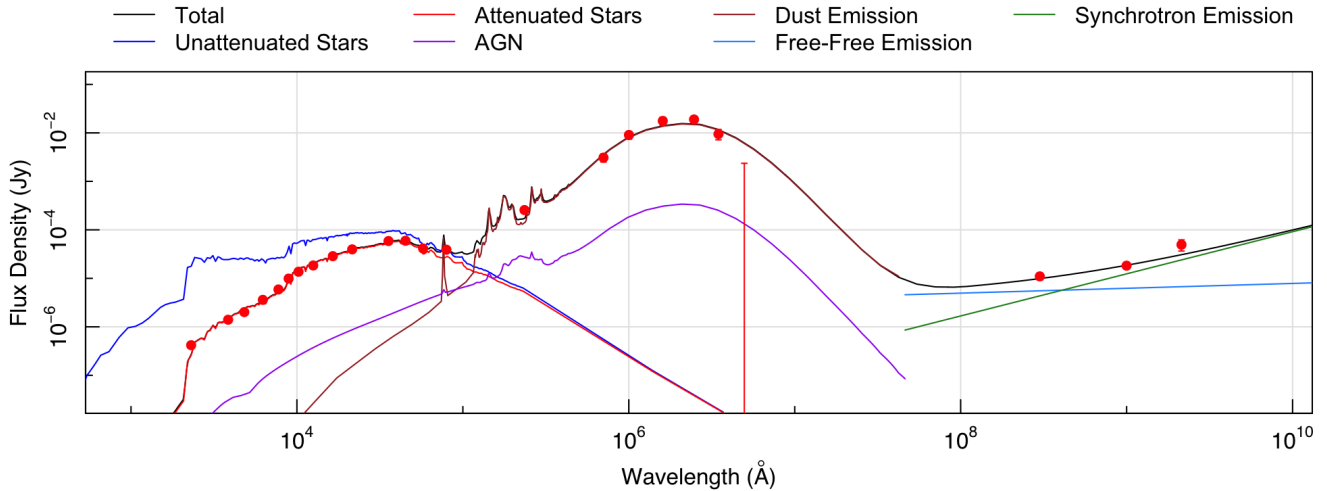


Figure 1. The resulting FUV–radio SED fit for DEVILS galaxy 101500680582617952. We show the input flux densities as the red points and error bars, and the total SED in black. The contributing components are also shown including the unattenuated stellar emission (blue), attenuated stellar emission (red), AGN component (purple), dust emission (brown), free-free emission (light blue), and synchrotron emission (green).

MCMC chain using the `LAPLACESDEMON`⁶ package. By alternating between the two different phases, `HIGHLANDER` is able to more efficiently sample the posterior parameter space, especially in scenarios that are highly multimodal, such as SED fitting, whilst still retaining the ability to extract uncertainties for each of the galaxy properties. Within `LAPLACESDEMON`, we utilize the `CHARM`⁷ algorithm using a Student-t likelihood. We fit with 2000 steps for both the genetic optimisation and MCMC phases, repeating each phase twice for a total of 8000 iterations. The values quoted within this work correspond to the maximum likelihood step and uncertainties are taken to be the 1σ range of the final MCMC phase. We include a 10 per cent error floor added in quadrature on all measurements to account for offsets between facilities and instruments.

3.3 ProSPECT Outputs

Figure 1 shows the input FUV–radio photometry for an example DEVILS galaxy, as well as the resulting ProSPECT fit and contributions from the stellar, dust, AGN, and radio free-free and synchrotron emission. In this case, the free-free emission is the dominant source of radio emission at 10 GHz and results in a bending in the radio-SED that would not be accounted for if fitting a single power law as in Dey et al. (2022).

The resulting SED for each galaxy is visually inspected to verify that the fit is appropriate and in general, the resulting SED fits are good especially for the KINGFISHER sample due to the greater photometric coverage. In addition, when converting the likelihoods to χ^2 values, all galaxies across DEVILS and KINGFISHER have a reduced $\chi^2 < 4$. For the DEVILS sample, the fits in the FIR regime are less constrained than the KINGFISHER galaxies due to lower SNR photometry. One such galaxy has radio emission at higher flux densities than the FUV–MIR and FIR photometry mostly consisting

of upper limits. This causes a discontinuity in the best-fitting SED at the point where the dominant emission mechanism shifts from the non-thermal radio continuum to emission from dust. This particular galaxy is classed as an RLAGN in the catalogue from Whittam et al. (2022) and radio jets can be seen in the 1.4 GHz image. This explains the very bright radio emission relative to the host galaxy.

Figure 2 shows the resulting SEDs for the sample of KINGFISHER galaxies sorted by stellar mass (each of the individual SEDs, component contributions, and resulting star formation and metallicity histories are made available as supplementary material). This Figure highlights the fact that the diversity in radio SEDs is observationally driven and is not just an unconstrained extension to the ProSPECT model.

4 RADIO SED PARAMETERS

The distributions of the ProSPECT parameters arising from the FUV–FIR portion of SEDs have been extensively explored in previous work (Bellstedt et al. 2020, 2021; Thorne et al. 2021, 2022a,b). However, to validate the implementation of the radio extension, this work explores the resulting radio-parameters and their correlations with other galaxy properties.

Figure 3 shows the distribution of the derived free-free fractions (f_{ff}) and synchrotron spectral indices (α_{sy}) as a function of redshift for our sample. Due to the very different redshift ranges sampled by the KINGFISHER and DEVILS samples, we show the distribution of just the KINGFISHER galaxies in the left panel, while the right panel shows the redshift distribution of both samples. For the DEVILS sample, we recover a median $f_{\text{ff}} = 0.05 \pm 0.007$ and $\alpha_{\text{sy}} = -0.84 \pm 0.05$. When removing the 14 galaxies identified as AGN by Whittam et al. (2022) or ProSPECT from the DEVILS sample, the median free-free fraction of the remaining 19 galaxies increases slightly to $f_{\text{ff}} = 0.055 \pm 0.007$ while the median synchrotron spectral index steepens slightly ($\alpha_{\text{sy}} = -0.9 \pm 0.07$) however, within errors these are still consistent with the full sample. For the sample of KINGFISHER galaxies, we recover a slightly higher median

⁶ <https://cran.r-project.org/web/packages/LaplacesDemon/index.html>

⁷ Component-wise hit and run metropolis.

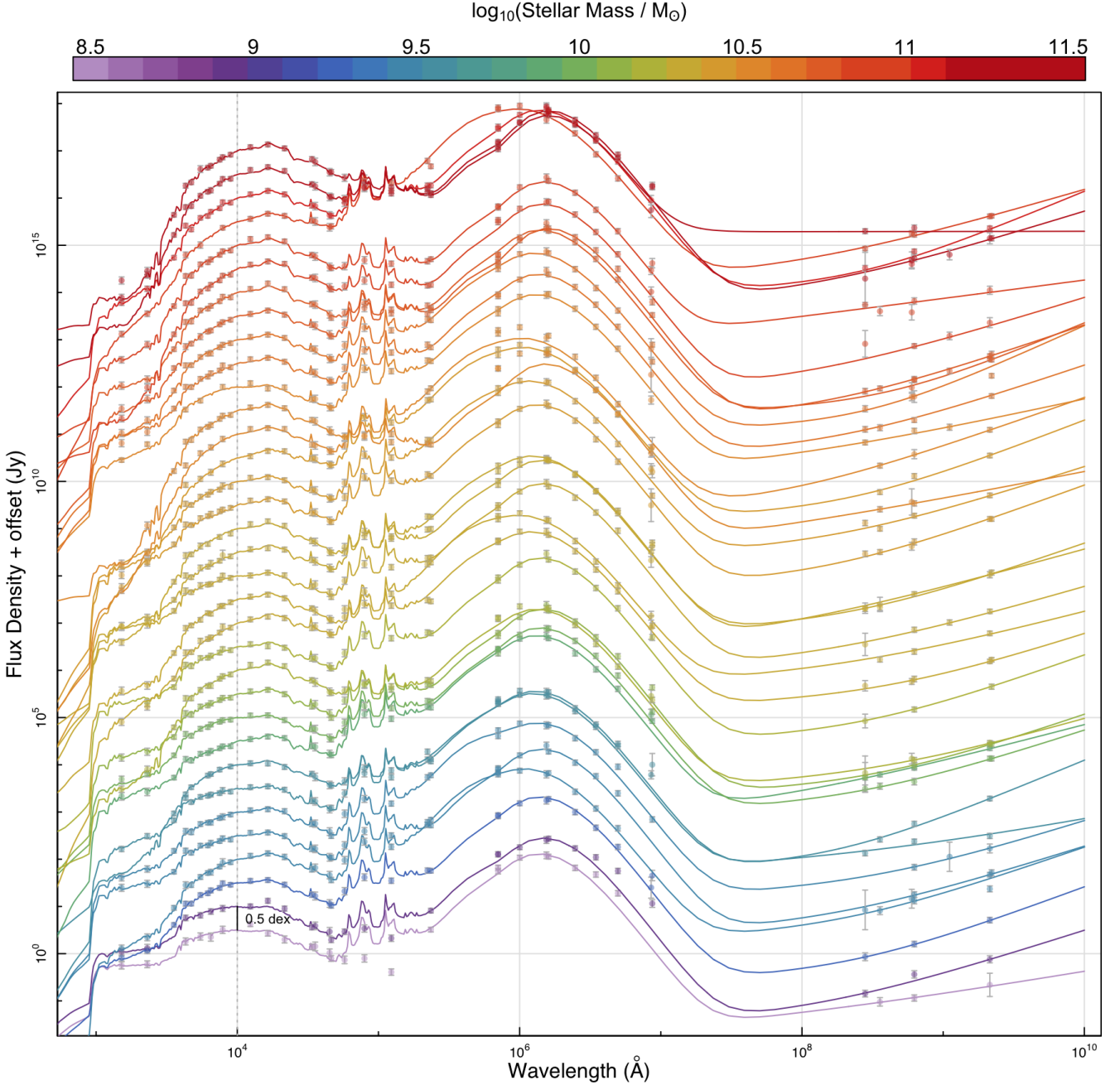


Figure 2. The input photometry (circles) and resulting PROSPECT fits for the sample of KINGFISHER galaxies sorted from least (purple) to most (red) massive as per the colour bar. To highlight the differences in SED between each galaxy we normalise each SED by the flux density at 10,000 Å and apply a fixed 0.5 dex offset.

$f_{\text{ff}} = 0.09 \pm 0.009$ than the DEVILS sample and a synchrotron spectral index $\alpha_{\text{sy}} = -0.98 \pm 0.03$. Our median free-free fraction for the KINGFISHER sample is consistent with those from surveys of nearby galaxies (8-10 per cent; Klein & Emerson 1981; Kennicutt 1983; Niklas et al. 1997). However, the median free-free fraction of the DEVILS sample is lower than previous estimations due to our sample selection not excluding AGN and could indicate that the RLAGN selection from Whittam et al. (2022) could be missing lower luminosity RLAGN. We recover a steeper synchrotron spectral index

than the canonically assumed value of $\alpha \sim -0.8$ (Condon 1992) and also steeper than the value derived by Klein & Emerson (1981); Niklas et al. (1997) as they included frequencies below 1 GHz where free-free absorption can cause a flattening of the SED (Lacki 2013; Calistro Rivera et al. 2017). However, our synchrotron spectral index is closer to that derived by Galvin et al. (2018), $\alpha_{\text{sy}} = -1.06$, who model the 70 MHz–48 GHz SEDs of 19 starburst galaxies and account for free-free emission and self-absorption as well as synchrotron emission. Our f_{ff} and α_{sy} values are also in agreement with

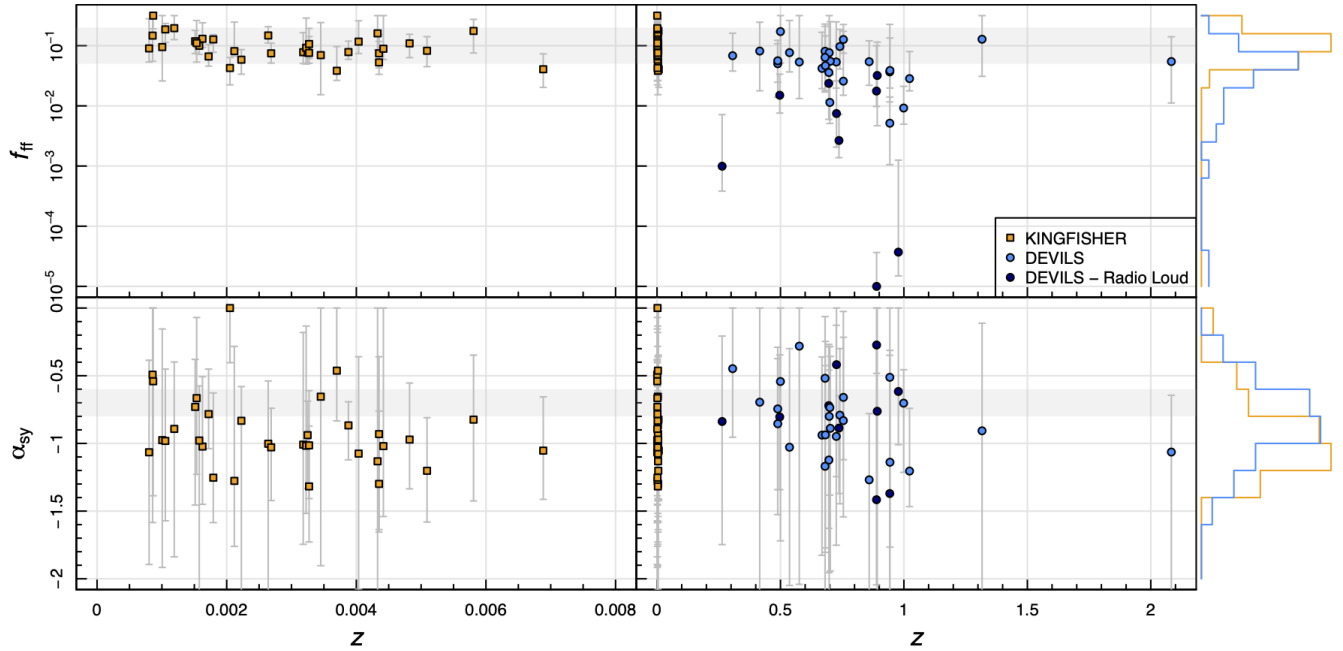


Figure 3. The distribution of recovered free-free fractions (f_{ff}) and synchrotron spectral index (α_{sy}) parameters as a function of redshift. The grey shaded region shows the expected ranges for the two parameters as per Condon (1992). We show the sample of KINGFISHER galaxies as the orange squares and the DEVILS sample as the blue circles. For the DEVILS sample, we show galaxies identified as radio-loud AGN by Whittam et al. (2022) as the navy blue circles. The right panel shows the full redshift range, while the left panel shows a zoom of the range covered by the KINGFISHER sample. The histograms on the outer right edge show the projected density of the recovered free-free fractions and synchrotron spectral indices for the two samples.

those from Tabatabaei et al. (2017) who also use the KINGFISHER sample and recover a mean $\alpha_{\text{nt}} = 0.97 \pm 0.16$ and $f_{\text{th}} = (10 \pm 9)$ per cent at 1.4 GHz.

We find no clear evolution in the free-free fraction or synchrotron spectral index as a function of redshift. However, we find that the median free-free fraction of the DEVILS sample is at the lower limit of the expected range from Condon (1992) and is lower than the median of the KINGFISHER sample. Of the DEVILS galaxies, we recover maximum likelihood free-free fractions below 0.05 for 16 of the 33 galaxies, with four of these galaxies with free-free fractions more than 3σ below $f_{\text{ff}} = 0.05$. For the KINGFISHER sample, only three of the 34 galaxies have a best-fitting free-free fraction below 0.05, however, in all three cases, the 1σ uncertainty is consistent with $f_{\text{ff}} = 0.05$. This trend is most likely driven by the differing selection of the two samples. While the KINGFISHER sample includes galaxies with an AGN nuclear type as derived from optical emission line diagnostic plots, these are all low-luminosity AGN except for NGC 1316 (Fornax A) which was not included in the radio observations from Tabatabaei et al. (2017) and is therefore not included in our final sample. On the other hand, our DEVILS sample selection did not remove AGN. Radio-loud AGN would be expected to have lower free-free fractions, therefore lowering the median f_{ff} value for the DEVILS sample. This is evident in the DEVILS source with $f_{\text{ff}} = 10^{-5}$ which lies at the lower limit of the allowed range and is classified as a radio-loud AGN based on the IRRC.

Figure 4 shows the two radio parameters plotted against each other with the ellipses showing the correlation from the final posterior chain. As expected, for each galaxy the f_{ff} and α_{sy} parameters are strongly correlated (evident as the diagonal trend in the ellipses) due to degeneracies when fitting where a flattening of the synchrotron spectrum is associated with an increase in free-free fraction

at 1.4 GHz. The correlation between f_{ff} and α_{sy} on a galaxy-by-galaxy basis is seen for both the KINGFISHER and DEVILS samples, however, the overall population values are not strongly correlated.

When fitting just the radio portion of a galaxy’s SED, the free-free fraction is difficult to derive as it relies on fitting over a wide frequency range to recover the change in slope at high frequencies from the increasing contribution from free-free emission. However, when simultaneously fitting the FUV-FIR SED, the value of normalisation of the free-free emission, and therefore the value of f_{ff} , can be more easily derived as it is coupled to the SFR and dust properties of the galaxy. The α_{sy} is only constrained by the radio measurements which are often impacted by differences between resolution, source detection, and flux density extraction techniques. These differences can lead to systematic flux density offsets between frequencies and therefore to poorly constrained spectral indices (see Appendix A for the impact of the large α_{sy} uncertainty on the resulting SED).

Figure 5 shows the distribution of the radio parameters as a function of stellar mass, SFR, and sSFR. In each case, we find no clear trend with either f_{ff} or α_{sy} . We find that the derived free-free fractions are typically in better agreement with the suggested values from Condon (1992) than the synchrotron spectral indices which show a large scatter within the allowed range.

Figure 6 shows the distribution of derived free-free fractions and synchrotron spectral indices as a function of the bolometric AGN luminosity (L_{AGN}) and f_{AGN} . When considering the distribution of recovered free-free fractions we find that most objects with practically no MIR contribution from an AGN ($f_{\text{AGN}} < 0.01$) have a free-free fraction consistent with expected values for ‘normal’ galaxies (0.05–0.2; Condon 1992). We also find that the radio-loud AGN all have a PROSPECT-derived $f_{\text{AGN}} > 0.02$, with a median $f_{\text{AGN}} = 0.13$. These objects also have $f_{\text{ff}} < 0.04$ corresponding to more radio emission

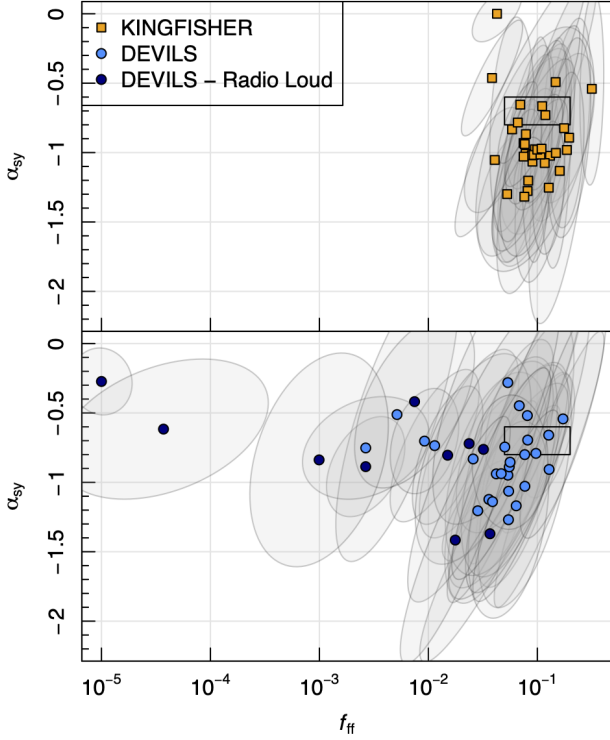


Figure 4. The synchrotron spectral index (α_{sy}) against the free-free fraction at 1.4 GHz (f_{ff}) for the KINGFISHER (upper) and DEVILS samples (lower). The ellipses show the correlation between the two parameters in the posterior chains. The black rectangle shows the expected range of the two parameters from Condon (1992).

than would be expected from star-formation alone (as per Condon 1992).

As our PROSPECT fits recover radio parameters (f_{ff} and α_{sy}) consistent with previous studies, and the free-free fractions of RLAGN behave as expected, we can be confident that our implementation does not obviously bias the recovery of radio parameters when simultaneously fitting FUV-radio SEDs.

4.1 Comparisons to Tabatabaei et al. (2017)

The SEDs of the KINGFISHER sample have been fit previously, however the FUV-FIR and radio regimes have only been considered separately. The radio SEDs of the KINGFISHER galaxies were previously fit by Tabatabaei et al. (2017) while the FUV-FIR SEDs were fit by Hunt et al. (2019). In this Section, we compare the estimates for the radio free-free fractions (f_{ff}) and synchrotron spectral indices (α_{sy}) as derived by PROSPECT to the results from Tabatabaei et al. (2017). We compare the results for other galaxy properties to those using MAGPHYS, CIGALE, and GRASIL from Hunt et al. (2019) in Appendix B. As discussed in Thorne et al. (2021) our flexible parametric SFH and evolving metallicity history implementation recovers systematically higher stellar masses than other codes that use variants of exponentially declining SFHs. We find that our dust luminosities are consistent with all three fitting techniques used by Hunt et al. (2019) however the recovered dust masses are highly dependent on the assumed mass to light conversions.

To fit the radio SEDs of the KINGFISHER galaxies, Tabatabaei

et al. (2017) use two power-law components to model the contribution from the free-free and synchrotron emission. Similarly to our PROSPECT fits, they also fix the slope of the free-free spectral index to -0.1 and fit for the synchrotron spectral index and the normalisations of the two components. The normalisations for each component were allowed to take negative values to test the robustness of the fit and to assess whether a free-free component was required. The two normalisation terms can be combined into a free-free fraction estimate at any frequency however we compare to the fractions derived at 20 cm (1.49 GHz). For five galaxies (IC0342, NGC 1482, NGC 3077, NGC 4236, and NGC 4579), Tabatabaei et al. (2017) found that two-component fits resulted in negative free-free fractions and so a single component was preferred. We do not include these galaxies in Figure 7.

Figure 7 shows the comparison of the two radio parameters derived with PROSPECT with the results from Tabatabaei et al. (2017). We find reasonable agreement between the free-free fractions, with a few objects offset by > 0.5 dex (NGC 2146, NGC 2798, NGC 3265, NGC 5713) however, within errors, these are consistent. Despite using the same allowed ranges, our α_{sy} values have a larger scatter when compared to Tabatabaei et al. (2017) than the free-free fractions. However, the derived spectral indices are relatively consistent with a median absolute offset of 0.17 with 90 per cent of the sample offset by less than 0.3.

We also show comparisons of the resulting fits in Figure 8 for three of the KINGFISHER galaxies (NGC 0628, NGC 1266, NGC 4569). The galaxies were selected to show a case where the best fitting radio parameters are in good agreement (NGC 0628), a case where they are in reasonable agreement (NGC 1266), and a case with the largest difference in synchrotron spectral index (NGC 4569). However, in all cases, the derived radio parameters are within errors and both the PROSPECT and Tabatabaei et al. (2017) fits provide a good fit to the data. Significant differences between the best-fitting total SEDs are not apparent within the frequency range examined here and determining the true shape of the radio SED would require additional measurements at higher frequencies.

These comparisons demonstrate that, even with the added complexity of simultaneously modeling the FUV-FIR, our derived radio parameters, and best-fitting radio SEDs are consistent with those derived using a simpler technique.

5 1.4 GHz LUMINOSITY – SFR RELATION

Using the PROSPECT fits for both the KINGFISHER and DEVILS samples we can also investigate the 1.4 GHz luminosity–SFR relation. The use of both DEVILS and KINGFISHER allows for a better sampling of the relation over a larger range of SFRs and luminosities, and to explore whether the relation evolves with redshift.

Figure 9 shows the relation using the PROSPECT-derived SFRs and the rest-frame 1.4 GHz luminosity derived using the associated best-fitting SED for both samples. We highlight sources that have been classed as RLAGN by Whittam et al. (2022) as the navy blue points. We find that most of our sample follow a tight relation, where a higher 1.4 GHz luminosity is associated with a higher SFR. However, we find that some galaxies lie below the relation. A number of these are identified as RLAGN by Whittam et al. (2022) or have very low SFRs indicative of passive systems (shown as the downward arrows). Interestingly, we find that the relationship is consistent between samples and shows no obvious discontinuity or change in slope between the KINGFISHER and DEVILS samples. This suggests no evolution in the relationship for $z < 1.5$.

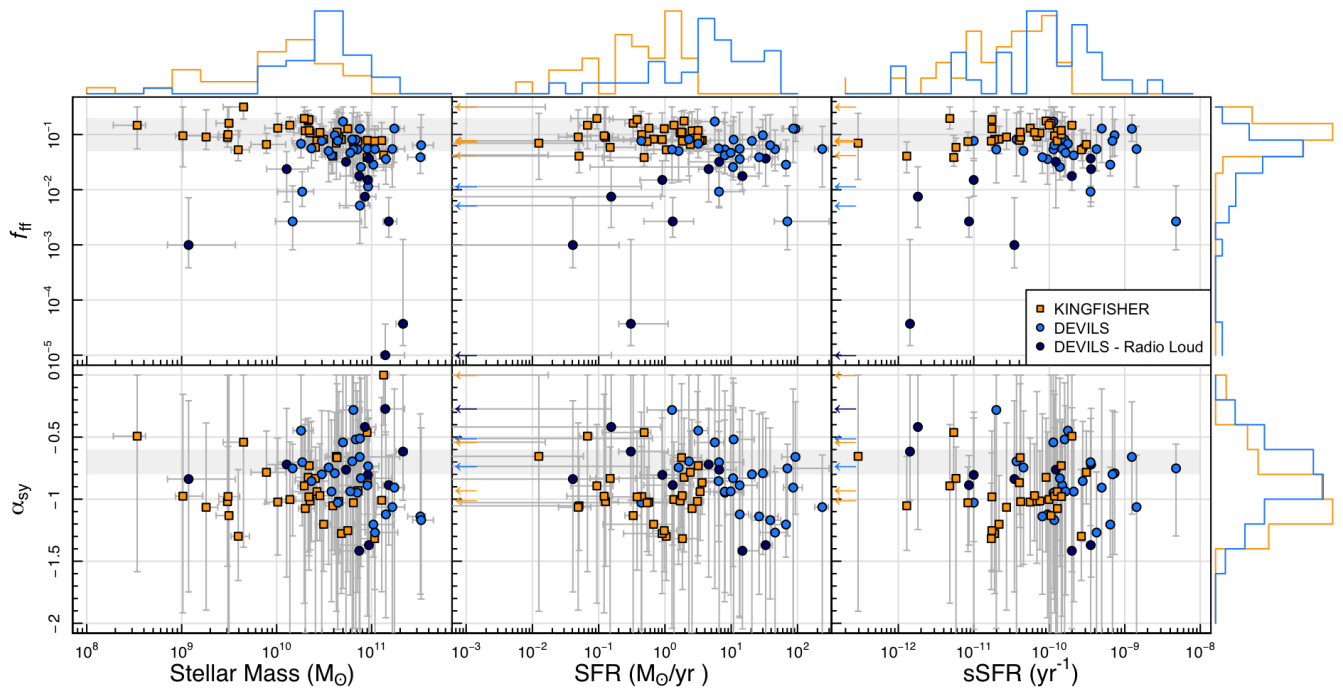


Figure 5. The distribution of recovered free-free fractions (f_{ff}) and synchrotron spectral index (α_{sy}) parameters as a function of stellar mass (left), SFR (middle), and sSFR (right). The colouring of points and grey shaded region are as per Figure 3. The outer histograms show the projected distribution of the KINGFISHER (orange) and DEVILS (blue) samples for each property.

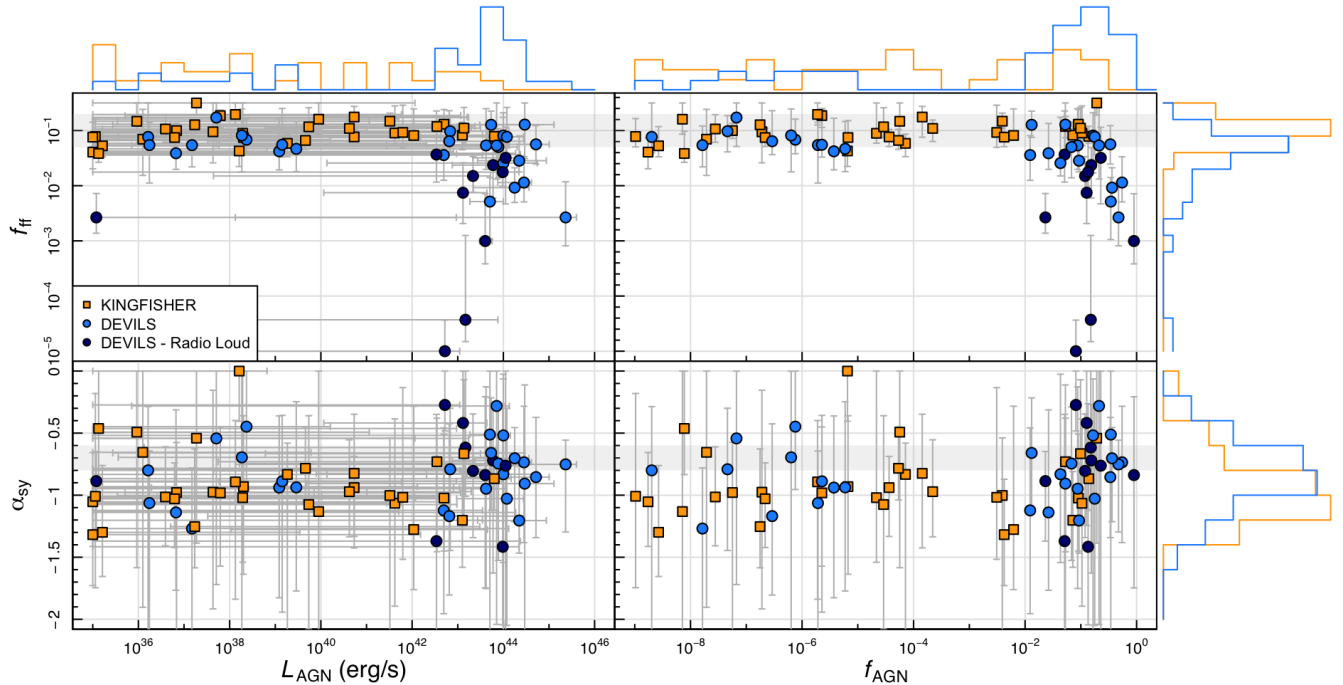


Figure 6. The distribution of recovered free-free fractions (f_{ff}) and synchrotron spectral index (α_{sy}) parameters as a function of AGN luminosity (left) and f_{AGN} (right). The colouring of points and grey shaded region are as per Figure 3. The outer histograms show the projected distribution of the KINGFISHER (orange) and DEVILS (blue) samples for each property.

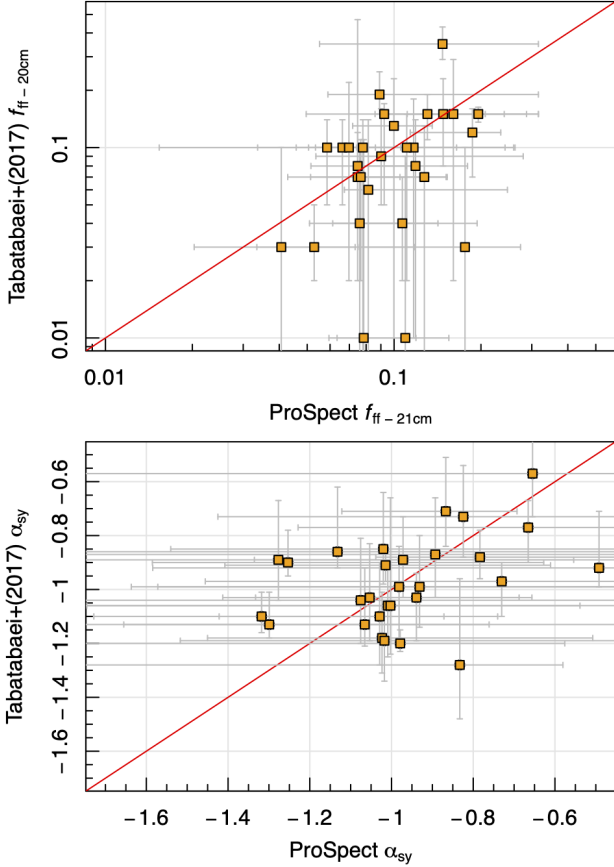


Figure 7. Comparisons of the derived free-free fractions and synchrotron spectral indices as derived by Tabatabaei et al. (2017) with those derived in this work for the KINGFISHER sample. The red line shows the one-to-one relation.

We show previously published relations outlined in Bell (2003), Condon (1992) Brown et al. (2017) as the dashed green, yellow, and grey lines respectively. We convert these to a Chabrier (2003) IMF using the conversions outlined in Haarsma et al. (2000) for Miller-Scalo to Salpeter, and Driver et al. (2013) for Salpeter to Chabrier. We also show the relations from Davies et al. (2017). These were derived using a combination of GAMA and the Faint Images of the Radio Sky at Twenty-cm (FIRST, Becker et al. 1995) surveys using both detections and stacking. The fits from Davies et al. (2017) shown in Figure 9 use MAGPHYS-derived SFRs and were performed using HYPERFIT using a fixed, $m = 1$, slope (blue line), and a free slope and normalisation (magenta).

Following the procedure from Davies et al. (2017) we also use HYPERFIT (Robotham & Obreschcow 2015) to fit the 1.4 GHz luminosity – SFR relation using a free slope and normalisation. We only include sources that are not identified as AGN by either Whittam et al. (2022) or PROSPECT (i.e. removing sources with $f_{\text{AGN}} > 0.1$). We also remove the two KINGFISHER galaxies with very low SFRs (where the 99.9th percentile of the SFR posterior is $< 10^{-5} M_{\odot} \text{ yr}^{-1}$) that lie significantly off the relation.

When fitting freely we derive a relationship between SFR and

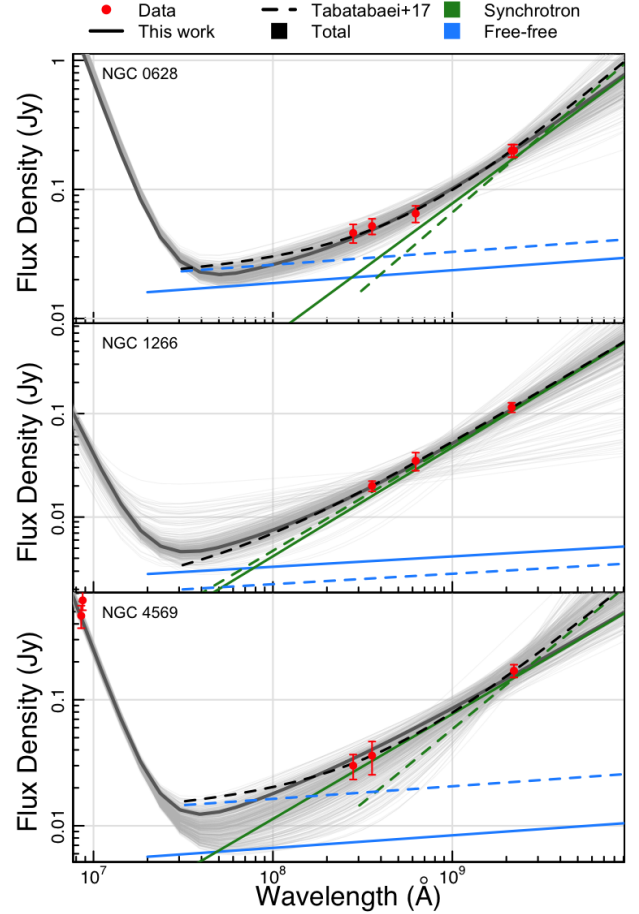


Figure 8. Comparisons of the radio SEDs for three example KINGFISHER galaxies (NGC 0628, NGC 1266, NGC 4569) obtained using PROSPECT with the fits from Tabatabaei et al. (2017). In each panel we show the input data (red points), both the free-free (blue) and synchrotron (green) contributions to the total radio continuum. In all cases, both the PROSPECT and Tabatabaei et al. (2017) fits provide a good fit to the data.

1.4 GHz luminosity given by:

$$\log_{10}(\text{SFR}/M_{\odot} \text{ yr}^{-1}) = (0.926 \pm 0.08) \times \log_{10}(L_{1.4 \text{ GHz}}/\text{W Hz}^{-1}) - (19.87 \pm 1.8). \quad (7)$$

We also fit assuming a unity slope which results in a best-fitting relation of

$$\log_{10}(\text{SFR}/M_{\odot} \text{ yr}^{-1}) = \log_{10}(L_{1.4 \text{ GHz}}/\text{W Hz}^{-1}) - (21.47 \pm 0.23). \quad (8)$$

Interestingly, within errors, the free and fixed slope fits are consistent. As free-free radio emission is known to scale linearly with SFR from the fundamental theory of emission processes (Condon 1992), this also suggests that synchrotron emission also scales linearly with SFR. This is contrary to the results of Davies et al. (2017) who recover a best-fitting relation with $m = 0.75 \pm 0.03$ suggesting that synchrotron emission does not scale linearly with star formation.

Although the derivation of both the SFR and 1.4 GHz rest-frame luminosity are linked, our findings are not a forced outcome of the model. The 1.4 GHz luminosity is dependent on the relative con-

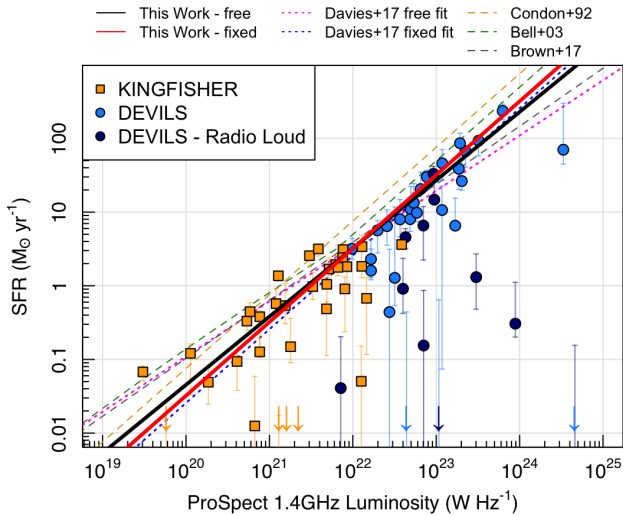


Figure 9. Correlation between 1.4 GHz luminosity and PROSPECT-derived SFR for the KINGFISHER (orange) and DEVILS (blue) samples. The dark blue indicates galaxies that were classed as RLAGN by Whittam et al. (2022). We show our linear fits with the free and fixed slopes as the black and red solid lines respectively. The free and fixed fits from Davies et al. (2017) are also shown as the dotted magenta and blue lines. We also show the relations from Condon (1992), Bell (2003) and Brown et al. (2017) as the dashed yellow, green, and grey lines respectively.

tributions of the free-free and synchrotron radio emission and the slope of the synchrotron component which are both modeled as free parameters in our implementation. Therefore, the relation given in Equation 7 provides an updated calibration to derived SFRs from rest-frame 1.4 GHz luminosities using a more robust SED fitting technique than those given in Davies et al. (2017).

6 USING THE RADIO CONTINUUM AS AN ANCHOR FOR ENERGY BALANCE

As we move into the era of the SKA and its precursors, the number of galaxies with radio data will significantly increase (e.g. the Evolutionary Map of the Universe; EMU, Norris et al. 2011, the Widefield ASKAP L-band Legacy All-sky Blind survey; WALLABY, Koribalski et al. 2020, the Rapid ASKAP Continuum Survey; RACS-mid, McConnell et al. 2020, and Deep Investigation of Neutral Gas Origins; DINGO, Meyer 2009). As there are no currently operating or planned future far-infrared observatories, there is no way to obtain FIR imaging of galaxies beyond what already exists, and as such techniques that rely on energy balance will be limited to higher redshifts (where the rest-frame FIR is pushed to millimeter wavelengths) or existing samples. However, due to the tight infrared–radio correlation, it is theoretically possible to use radio continuum emission to constrain the re-emission of processed stellar light by dust instead of the FIR. As such, here we explore the potential of using the radio continuum for energy balance when the FIR is unavailable. Using the DEVILS and KINGFISHER sample of galaxies we explore the utility of including the radio continuum as an anchor for energy balance in the absence of FIR data.

As discussed in Thorne et al. (2022a), FIR photometry is required when SED fitting to constrain a MIR AGN component. As we are removing FIR photometry in this section we limit our DEVILS sample

to only galaxies with $f_{\text{AGN}} < 0.1$ from our PROSPECT fits and exclude the AGN component from our PROSPECT fits (i.e. set $\text{AGNlum} = 0$).

To help constrain the fit to the radio data we implement a prior on the synchrotron spectral index of:

$$\exp\left(-\frac{1}{2}\left(\frac{\alpha_{\text{sy}} - 0.9}{0.2}\right)^2\right), \quad (9)$$

where the values for the mean and standard deviation were informed by the distribution of values obtained for the DEVILS and KINGFISHER samples in Section 4. We also implement a prior on the free-free fraction as given by:

$$\exp\left(-\frac{1}{2}\left(\frac{\log_{10}(f_{\text{ff}}) + \log_{10}(0.08)}{0.3}\right)^2\right). \quad (10)$$

This corresponds to a mean free-free fraction of 0.08 and a 1σ range spanning $\sim 0.05 - 0.20$ as suggested by (Condon 1992).

Using this implementation we explore two scenarios. In the first, we remove all photometry between 24–850 micron (i.e. MIPS 24 - HFI/SCUBA 850 μm bands) and limit our radio coverage to just a single measurement at 1.4 GHz. We choose 1.4 GHz as this is the frequency of a number of SKA precursor surveys such as the MIGHTEE, WALLABY, RACS-mid, and DINGO surveys and as such will provide 1.4 GHz continuum measurements covering a very large area. In this scenario, both samples have good coverage from the FUV-MIR, especially the KINGFISHER sample, allowing for reasonable constraint on balance between attenuated and re-emitted energy. We also explore a more extreme scenario where only optical and NIR photometry is available. In practice, this is implemented by removing measurements at wavelengths longer than IRAC 1 and also removing GALEX UV measurements. This is closer to what might be expected outside panchromatic survey fields, but where estimates for the properties of the host galaxies of transient events are still required (e.g. Seymour et al. 2020; Norris et al. 2022).

6.1 Where FUV-MIR data are available

To test the utility in including a radio continuum measurement where FIR data are not available we re-fit our galaxy samples removing all FIR photometry between 24–850 μm (i.e. MIPS 24 - HFI/SCUBA 850 μm bands) and using only the available measurements at 1.4 GHz. For a control sample, we also re-fit our sample using only the available FUV-MIR data with no FIR or radio data included. To evaluate the improvement when including the 1.4 GHz measurement we compare to the galaxy properties as derived using the full FUV-radio fits as described in Section 3.

Figure 10 presents comparisons of the probability distributions for the derived stellar masses, SFRs, and dust luminosities when fitting with different wavelength sampling. The red shows the case where no FIR or radio data is being used to constrain the dust emission element of the energy balance, while the blue shows the case where we have included a 1.4 GHz measurement in the fit. The x -axis in these figures is the offset from the parameter derived using the fitting process applied using the full available FUV-radio coverage. To calculate these differences, for each galaxy and parameter, we randomly sample the posterior 1000 times for both the full and reduced photometry iterations. This highlights not only the impact on the single best-fitting value but also the distribution of sampled values and therefore the uncertainty on each parameter. We find that for the KINGFISHER sample, the addition of the 1.4 GHz measurement makes little difference in the recovery of the SFRs and dust luminosities, but does allow for a slightly tighter recovery of stellar masses. However, for

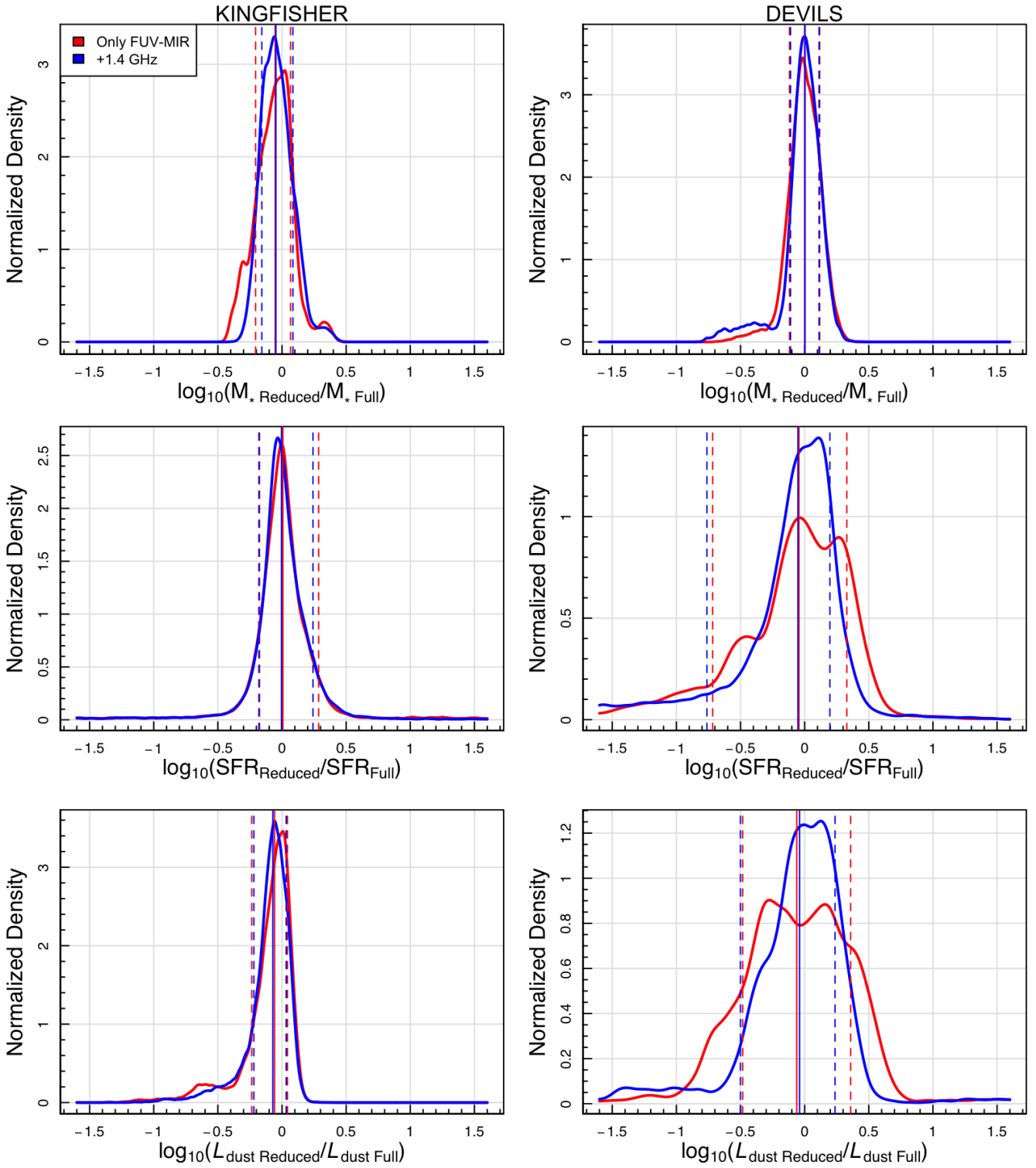


Figure 10. Difference between probability distributions for the stellar mass (top), SFR (middle), and dust luminosity (bottom) derived using the FUV-MIR (red) and FUV-MIR+1.4 GHz (blue) iterations relative to the probability distributions derived using the full FUV-radio photometry coverage. Due to differences in photometry coverage we show the KINGFISHER (left) and DEVILS (right) samples separately. In each panel the solid line shows the median offset while the 16th and 84th percentiles are shown as the dashed line.

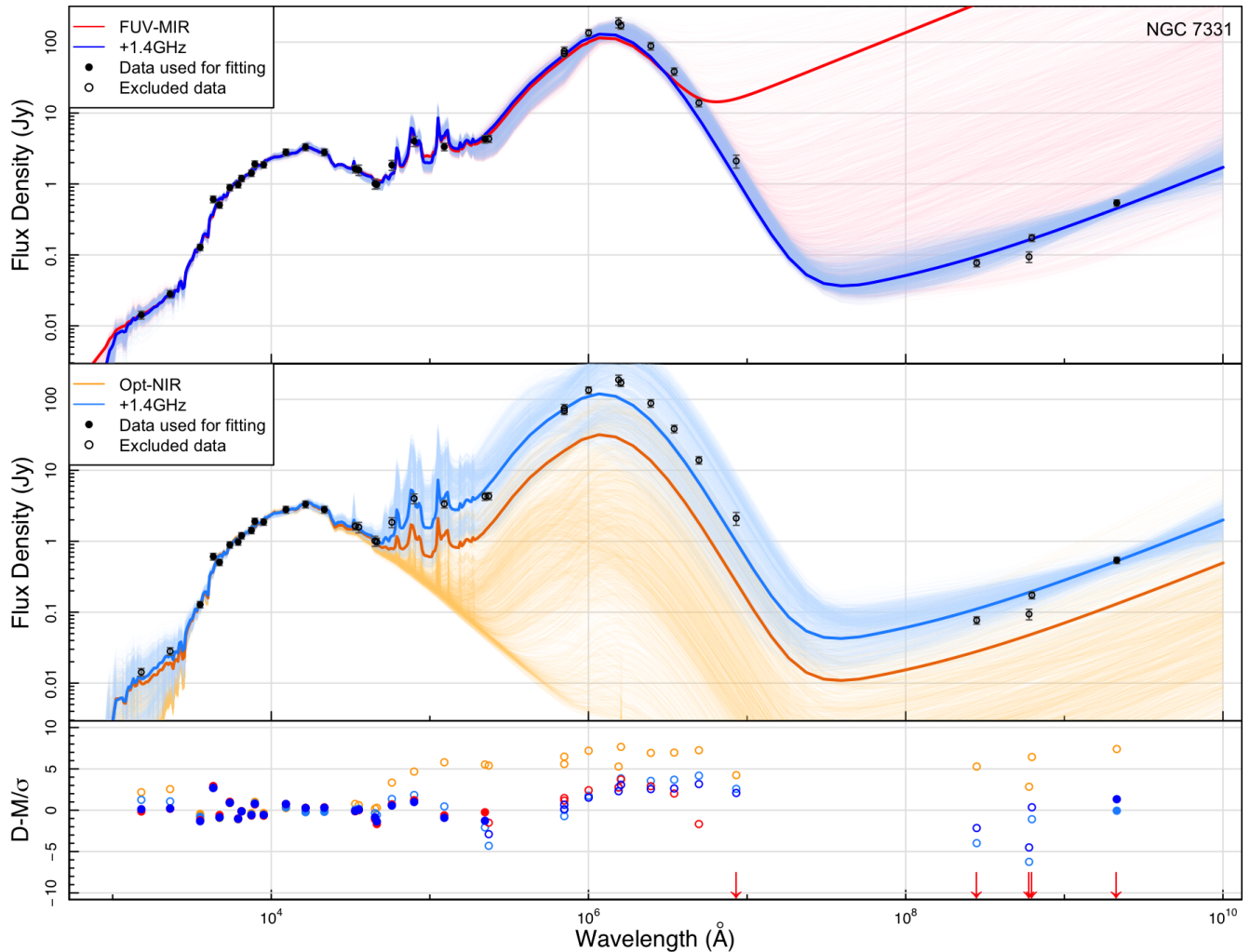


Figure 11. Comparisons of the SED fitting results for NGC 7331 when only FUV-MIR (top, red) or optical-NIR (middle, orange) is used versus when a 1.4 GHz measurement is also included (blue). In each panel, the dark line shows the best fitting (maximum likelihood) SED, while the lighter coloured lines show the sampling of the final MCMC chain. The upper and middle panels show the input photometry for the fits (solid circles) and the photometry that was excluded from the fit for testing purposes (open circles). The lower panel shows the relative offset (data - model / error) of each data point from the best-fitting SEDs derived using the different input data.

the DEVILS sample, the inclusion of a 1.4 GHz measurement results in a median offset closer to zero for both the SFR and dust luminosity and results in a tighter distribution.

The differences in impact between the two surveys can be explained by the excellent wavelength coverage in the MIR for the KINGFISHER sample. By combining four WISE channels with four IRAC channels, the SED fits for the KINGFISHER sample are well constrained in the MIR allowing for good constraint on the dust luminosity and SFR. However, as there is less MIR wavelength coverage for DEVILS and the photometry has lower SNR, the inclusion of a 1.4 GHz measurement allows for better recovery of the SFRs and dust luminosities.

These results suggest that in the absence of FIR photometry, the inclusion of a radio continuum measurement with well-chosen priors can aid in constraining the emission from dust and therefore lead to more accurate estimates of SFR and dust luminosity where FIR data is limited or of low SNR. However, the offsets in this scenario are quite moderate.

6.2 Where only optical-NIR data are available

We also explore a more extreme scenario where only optical-NIR photometry is available and a MIR constraint on dust emission is not possible. We implement this by removing the *GALEX* UV measurements and all photometry between 3.6 - 850 μm (IRAC 1 - SCUBA/HFI 850 μm). As per Section 6.1, we also fit using just the optical-NIR data as a control sample for comparison. Figure 11 shows the best-fitting SEDs derived for NGC 7331 when only FUV-MIR (upper panel) and optical-NIR (middle panel) photometry is used versus when a 1.4 GHz measurement is also incorporated. We find that when including the 1.4 GHz radio measurement, the derived SED is in closer agreement with the excluded data, especially in the MIR and FIR. Though we only show one example here, we find that generally the addition of the 1.4 GHz measurement results in a best-fitting SED that more closely resembles the actual SED of the galaxy. However, in some galaxies, the difference between SEDs is not as large as in the example shown here.

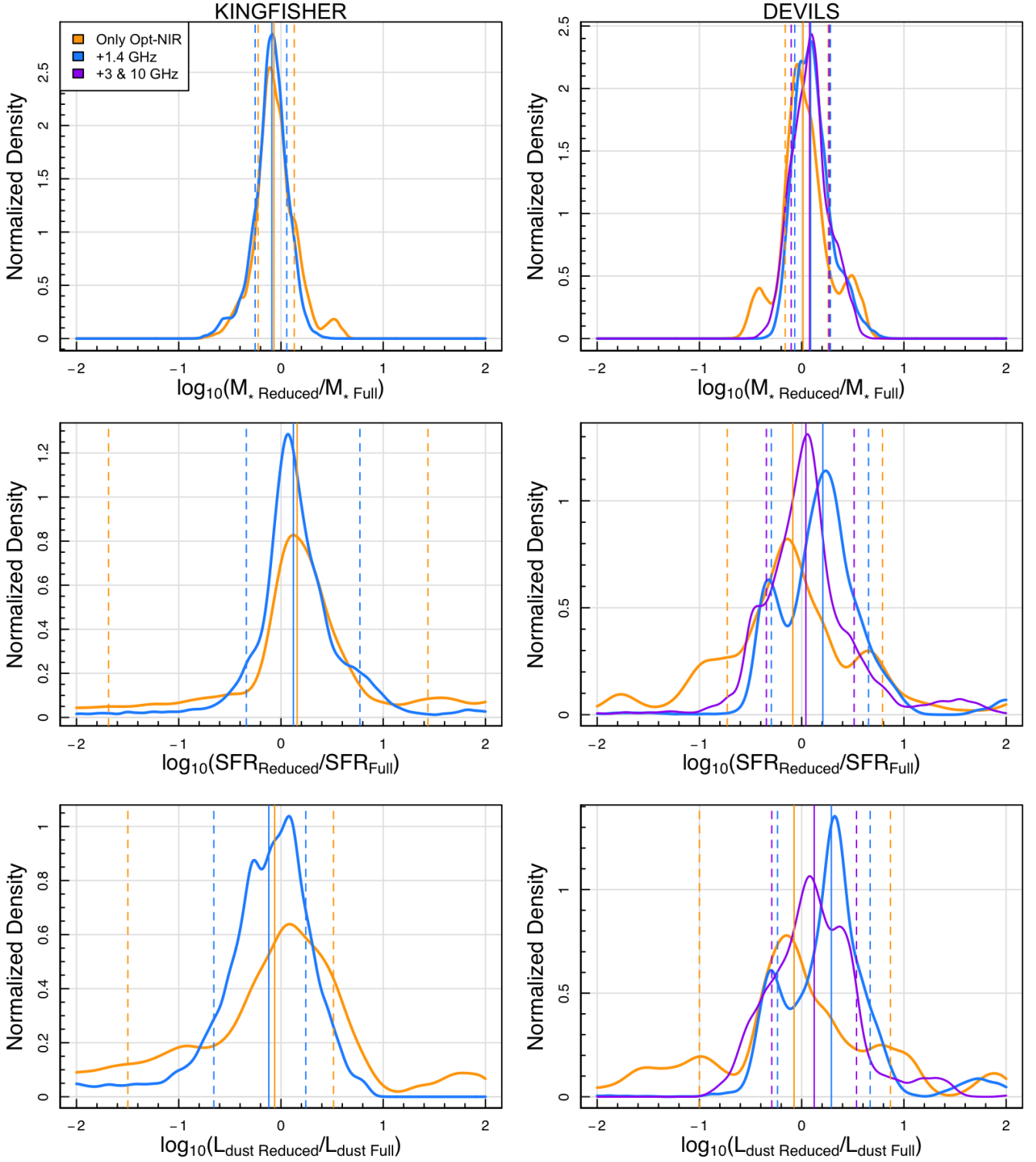


Figure 12. Difference between probability distributions for the stellar mass (top), SFR (middle), and dust luminosity (bottom) derived using the optical-NIR (orange), optical-NIR+1.4 GHz (light blue), and optical-NIR+1.4,3,10 GHz (purple - DEVILS only) iterations relative to the probability distribution derived using the full FUV-radio photometry coverage. Due to differences in photometry coverage we show the KINGFISHER (left) and DEVILS (right) samples separately. In each panel, the solid line shows the median offset while the 16th and 84th percentiles are shown as the dashed line.

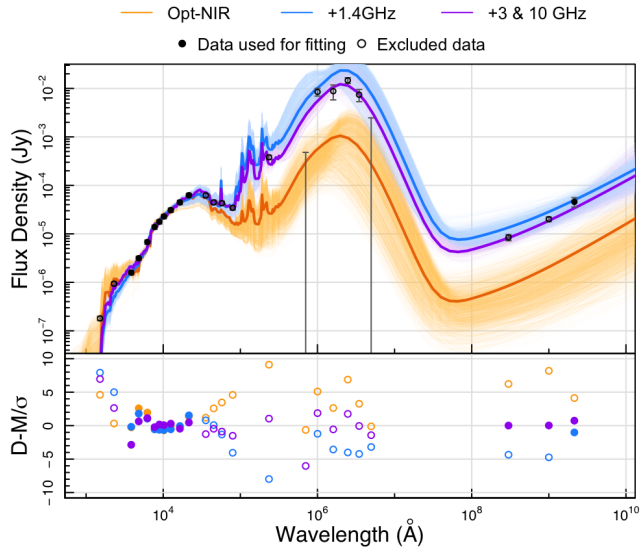


Figure 13. Comparisons of the SED fitting results for an example DEVILS galaxy (101500953042568112) when only the optical-NIR (orange) is used versus when a 1.4 GHz measurement (blue) or measurements at 1.4, 3, and 10 GHz are included (purple). The upper panel shows the input photometry for the fits (solid circles) and the photometry that was excluded from the fit for testing purposes (open circles). The lower panel shows the relative offset (data - model / error) of each data point from the best-fitting SEDs derived using the different input data.

Figure 12 presents comparisons of the derived stellar masses, SFRs, and dust luminosities when fitting with only the optical-NIR versus fitting with optical-NIR and 1.4 GHz measurement and is calculated as per Figure 10. In this scenario, we find that the addition of a 1.4 GHz measurement results in tighter distributions for the SFR and dust luminosity for both DEVILS and KINGFISHER. However, it also increases the median offset for the dust luminosities, and for the DEVILS SFR. However, these changes in offset are small and within the typical errors for each parameter when fitting with better wavelength coverage.

We also find that the inclusion of a flux density measurement at 1.4 GHz decreases the median uncertainty on derived SFRs by 0.1 dex for both DEVILS and KINGFISHER (from 0.55 to 0.45 dex for KINGFISHER and from 0.35 to 0.25 dex for DEVILS where in both cases the median uncertainty when including all FUV-radio data is ~ 0.2 dex). Similarly, the inclusion of a 1.4 GHz measurement decreases the median uncertainty on derived dust luminosities 0.2 dex (from 0.84 to 0.64) for KINGFISHER and 0.14 dex for DEVILS (from 0.41 to 0.27 dex).

6.2.1 Incorporating additional radio data

We also explore the constraint provided by including additional radio data in addition to a 1.4 GHz measurement. To do this we elect to use only the DEVILS sample as the frequency coverage for all galaxies is uniform (i.e. measurements at 1.4, 3, and 10 GHz for all galaxies). We explore the situation where only optical and NIR data are available and re-fit the SEDs of the DEVILS galaxies incorporating all three radio measurements. As the increased coverage at radio frequencies allows for additional constraint on the two radio parameters (α_{sy} and f_{ff}), we adapt the imposed priors as described in Equations 9 and 10

to be less restrictive by increasing the standard deviations from 0.2 and 0.3 to 0.4 and 0.5 for the α_{sy} and f_{ff} parameters respectively.

Figure 13 shows the impact for an example DEVILS galaxy where the fit obtained using just the optical-NIR data is shown in orange, the fit using an additional 1.4 GHz measurement is shown in blue, and the addition of all three radio measurements is shown in purple. It is clear that the inclusion of even just the 1.4 GHz measurement provides substantial improvement in recovering a best-fitting SED consistent with the observed FIR data, however, the incorporation of the additional measurements at 3 and 10 GHz provides the best match to the observed MIR and FIR. We show the impact of including additional radio measurements on the derived galaxy properties as the purple line in Figure 12. While the inclusion of the 3 and 10 GHz measurements makes little difference to the derivation of stellar masses, it does result in a tighter distribution for the SFRs and dust luminosities despite the less restrictive prior.

Along with the results from the previous Section, these comparisons highlight the utility of including at least one radio continuum measurement to improve the accuracy of derived galaxy SEDs and properties. This will be especially important in the era of the SKA where large all-sky surveys will target regions with sparse optical-NIR photometric coverage but will still require accurate estimates of galaxy properties such as SFR and dust luminosities.

7 SUMMARY

In this work, we have extended the PROSPECT SED-fitting code to simultaneously model the FUV-FIR regimes and the radio-continuum, incorporating both the free-free and synchrotron components. We have applied this extended version of PROSPECT to a sample of 30 galaxies from the DEVILS sample and 34 KINGFISHER galaxies to explore the impact of modeling the full FUV-radio SEDs of galaxies.

We derive free-free fractions (f_{ff}) and synchrotron spectral indices (α_{sy}) for all of our galaxies and find that they are in reasonable agreement with estimates derived when fitting only at radio frequencies from Tabatabaei et al. (2017). We recover a median free-free fraction at 1.4 GHz of 0.05 ± 0.03 and 0.09 ± 0.04 and a median synchrotron spectral index of -0.84 ± 0.29 and -0.98 ± 0.22 for the DEVILS and KINGFISHER samples respectively. We also find that objects with very low free-free fractions, suggesting higher synchrotron contributions, are also identified as radio-loud AGN using the infrared-radio correlation (Whittam et al. 2022). These objects are also often associated with higher contributions from an AGN component in the mid-infrared.

We explore the relationship between SFR and rest-frame 1.4 GHz luminosity and find that most of our sample follows a tight relation, where a higher 1.4 GHz luminosity is associated with a higher SFR. This is in agreement with previous results from Condon (1992); Bell (2003); Brown et al. (2017) and Davies et al. (2017) at low- z . We also find that the relationship is consistent between the DEVILS and KINGFISHER samples with no obvious discontinuity or change in slope, suggesting no evolution in the relationship for $z < 1.5$. We recover a steeper slope than Davies et al. (2017) of $m = 0.925 \pm 0.08$ consistent with a linear relationship between SFR and 1.4 luminosity. This suggests that emission from both the free-free and synchrotron components scales linearly with star formation.

Additionally, as the radio continuum extension to PROSPECT is parameterised using the relationship between far-infrared and free-free emission, we find that the radio continuum can be a reasonable substitute for FIR photometry for the purposes of energy balance. We find that the incorporation of radio continuum data is especially use-

ful in improving the accuracy of derived SFRs and dust luminosities in situations where only optical-NIR photometry would be available otherwise. This finding is valuable due to the lack of operating and planned far-infrared observatories and to the upcoming plethora of data from the SKA and its precursors (ASKAP and MeerKAT, Meyer 2009; Norris et al. 2011; Jarvis et al. 2016; Koribalski et al. 2020; McConnell et al. 2020). We also demonstrate that including additional radio measurements (in this case at 3 and 10 GHz) allows for additional constraint on the energy balance and therefore the SFR and dust luminosity. We recommend that, in situations where FIR data is not available, the radio continuum be used to aid in constraining the energy balance and therefore SFRs and dust luminosities. This can be implemented either using a single radio measurement with informative priors for the radio parameters or using measurements at multiple radio frequencies with less restrictive or uniform priors.

In addition to the benefits outlined above, extending FUV-FIR SED fitting techniques to radio frequencies, even in a predictive mode, could be used to improve radio source-finding techniques and could aid in associating radio sources with optical counterparts. We have demonstrated that for normal galaxies, the derived free-free fractions are relatively constant with redshift and other galaxy properties. Hence, using default values ($f_{\text{ff}} = 0.1$ and $\alpha_{\text{sy}} = -0.8$), PROSPECT could be used to predict the radio emission from a given SED fit which could be used alongside positional information to correctly associate radio sources with their optical counterpart. Additionally, if sources lacking FIR photometry have significantly more radio emission than predicted by PROSPECT, this could be used to identify radio-loud AGN in situations where the infrared–radio correlation cannot be used directly. These scenarios all highlight the potential advantages of simultaneous and self-consistent consideration of the FUV-radio SEDs of galaxies.

Although this work considers only radio frequencies above 1.3 GHz, the radio frequency coverage in PROSPECT could be extended to model radio emission at lower frequencies (i.e. ~ 150 MHz from surveys such as the Low Frequency Array (LOFAR) Two Metre Sky Survey; LOTSS Smith et al. 2021; Shimwell et al. 2022; Heesen et al. 2022). However, to do this, PROSPECT may need to be adapted to account for potential flattening of the radio continuum below ~ 1 GHz (Condon 1992; Delhaize et al. 2017; Galvin et al. 2018; Dey et al. 2022).

ACKNOWLEDGEMENTS

We thank the anonymous referee for their constructive report. JET is supported by the Australian Government Research Training Program (RTP) Scholarship. ASGR and LJMD acknowledge support from the *Australian Research Council's* Future Fellowship scheme (FT200100375 and FT200100055 respectively). SB acknowledges support from the *Australian Research Council's* Discovery Project and Future Fellowship funding schemes (DP180103740, FT200100375).

We acknowledge the traditional owners of the land on which this research was completed, the Whadjuk Noongar people, and the land on which the AAT stands, the Gamilaraay people, and pay our respects to elders past and present.

DEVILS is an Australian project based around a spectroscopic campaign using the Anglo-Australian Telescope. The DEVILS input catalogue is generated from data taken as part of the ESO VISTA-VIDEO (Jarvis et al. 2013) and UltraVISTA (McCracken et al. 2012) surveys. DEVILS is part funded via Discovery Programs by the Australian Research Council and the participating in-

stitutions. The DEVILS website is <https://devilsurvey.org>. The DEVILS data is hosted and provided by AAO Data Central (<https://datacentral.org.au/>).

This work was supported by resources provided by the Pawsey Supercomputing Centre with funding from the Australian Government and the Government of Western Australia.

All of the work presented here was made possible by the free and open R software environment (R Core Team 2020). All figures in this paper were made using the R MAGICAXIS package (Robotham 2016b). This work also makes use of the CELESTIAL package (Robotham 2016a).

DATA AVAILABILITY

The DEVILS data products used in this paper are presented in Davies et al. (2021), Thorne et al. (2021) and Thorne et al. (2022a). They will be made publicly available as part of the DEVILS first data release described in Davies et al. (in preparation). The galaxy properties derived in this work for the KINGFISHER sample are available in Appendix A and made available as supplementary material. We also make available individual figures for each KINGFISHER galaxy showing the best fitting SED and the resulting star formation and metallicity history. Any other outputs for the KINGFISHER sample will be made available upon reasonable request to the corresponding author.

REFERENCES

- Aihara H., et al., 2019, *PASJ*, 71, 114
 Alam S., et al., 2015, *ApJS*, 219, 12
 Algera H. S. B., et al., 2020, *ApJ*, 903, 139
 Becker R. H., White R. L., Helfand D. J., 1995, *ApJ*, 450, 559
 Bell E. F., 2003, *ApJ*, 586, 794
 Bell E. F., McIntosh D. H., Katz N., Weinberg M. D., 2003, *ApJS*, 149, 289
 Bell E. F., et al., 2005, *ApJ*, 625, 23
 Bellstedt S., et al., 2020, *MNRAS*, 498, 5581
 Bellstedt S., et al., 2021, *MNRAS*, 503, 3309
 Boquien M., Burgarella D., Roehlly Y., Buat V., Ciesla L., Corre D., Inoue A. K., Salas H., 2019, *A&A*, 622, A103
 Brown M. J. I., et al., 2017, *ApJ*, 847, 136
 Bruzual G., Charlot S., 2003, *MNRAS*, 344, 1000
 Calistro Rivera G., et al., 2017, *MNRAS*, 469, 3468
 Calzetti D., Armus L., Bohlin R. C., Kinney A. L., Koornneef J., Storchi-Bergmann T., 2000, *ApJ*, 533, 682
 Capak P., et al., 2007, *ApJS*, 172, 99
 Carnall A. C., McLure R. J., Dunlop J. S., Davé R., 2018, *MNRAS*, 480, 4379
 Chabrier G., 2003, *PASP*, 115, 763
 Charlot S., Fall S. M., 2000, *ApJ*, 539, 718
 Chevillard J., Charlot S., 2016, *MNRAS*, 462, 1415
 Condon J. J., 1992, *ARA&A*, 30, 575
 Condon J. J., Yin Q. F., 1990, *ApJ*, 357, 97
 Condon J. J., Cotton W. D., Broderick J. J., 2002, *Astron. J.*, 124, 675
 Conroy C., 2013, *ARA&A*, 51, 393
 Da Cunha E., Charlot S., Elbaz D., 2008, *MNRAS*, 388, 1595
 Dale D. A., et al., 2005, *ApJ*, 633, 857
 Dale D. A., et al., 2007, *ApJ*, 655, 863
 Dale D. A., et al., 2012, *ApJ*, 745, 95
 Dale D. A., Helou G., Magdis G. E., Armus L., Díaz-Santos T., Shi Y., 2014, *ApJ*, 784, 83
 Dale D. A., et al., 2017, *ApJ*, 837, 90
 Davies L. J. M., et al., 2017, *MNRAS*, 466, 2312
 Davies L. J. M., et al., 2018, *MNRAS*, 480, 768
 Davies L. J. M., et al., 2021, *MNRAS*, 506, 256

- Delhaize J., et al., 2017, *A&A*, 602, A4
- Delvecchio I., et al., 2021, *A&A*, 647, A123
- Dey S., Goyal A., Malek K., Galvin T. J., Seymour N., Santos T. D., Piotrowska J., Charmandaris V., 2022, *ApJ*, 938, 152
- Draine B. T., 2003, *ARA&A*, 41, 241
- Draine B. T., et al., 2007, *ApJ*, 663, 866
- Draine B. T., et al., 2014, *ApJ*, 780, 172
- Driver S. P., Robotham A. S. G., Bland-Hawthorn J., Brown M., Hopkins A., Liske J., Phillipps S., Wilkins S., 2013, *MNRAS*, 430, 2622
- Drouart G., et al., 2021, *PASA*, 38, e049
- Feltré A., Hatziminaoglou E., Fritz J., Franceschini A., 2012, *MNRAS*, 426, 120
- Fioc M., Rocca-Volmerange B., 2019, *A&A*, 623, A143
- Fitzpatrick E. L., 1999, *PASP*, 111, 63
- Fritz J., Franceschini A., Hatziminaoglou E., 2006, *MNRAS*, 366, 767
- Galvin T. J., et al., 2018, *MNRAS*, 474, 779
- Gil de Paz A., et al., 2007, *ApJS*, 173, 185
- Gürkan G., et al., 2018, *MNRAS*, 475, 3010
- Haarsma D. B., Partridge R. B., Windhorst R. A., Richards E. A., 2000, *ApJ*, 544, 641
- Harwit M., Pacini F., 1975, *ApJ*, 200, L127
- Heesen V., et al., 2022, *A&A*, 664, A83
- Heywood I., et al., 2022, *Mon. Not. R. Astron. Soc.*, 509, 2150
- Holland W. S., et al., 1999, *MNRAS*, 303, 659
- Hopkins A. M., et al., 2003, *ApJ*, 599, 971
- Hunt L. K., et al., 2019, *A&A*, 621, A51
- Jarrett T. H., Chester T., Cutri R., Schneider S. E., Huchra J. P., 2003, *AJ*, 125, 525
- Jarrett T. H., et al., 2013, *AJ*, 145, 6
- Jarvis M. J., et al., 2013, *MNRAS*, 428, 1281
- Jarvis M., et al., 2016, The MeerKAT International GHz Tiered Extragalactic Exploration (MIGHTEE) Survey. eprint: arXiv:1709.01901
- Johnson B. D., Leja J., Conroy C., Speagle J. S., 2021, *ApJS*, 254, 22
- Kennicutt R., 1983, *Astron. Astrophys. Vol 120 P 219-222 1983*, 120, 219
- Kennicutt Jr. R. C., 1998, *ApJ*, 498, 541
- Kennicutt R. C., Evans N. J., 2012, *ARA&A*, 50, 531
- Kennicutt Jr. R. C., et al., 2003, *PASP*, 115, 928
- Kennicutt R. C., et al., 2011, *PASP*, 123, 1347
- Klein U., Emerson D. T., 1981, *A&A*, 94, 29
- Koribalski B. S., et al., 2020, *Astrophys. Space Sci.*, 365, 118
- Lacki B. C., 2013, *MNRAS*, 431, 3003
- Laigle C., et al., 2016, *ApJS*, 224, 24
- Laor A., Draine B. T., 1993, *ApJ*, 402, 441
- Lower S., Narayanan D., Leja J., Johnson B. D., Conroy C., Davé R., 2022, *ApJ*, 931, 14
- Lutz D., et al., 2011, *A&A*, 532, A90
- Maddox N., et al., 2021, *A&A*, 646, A35
- Marvil J., Owen F., Eilek J., 2015, *AJ*, 149, 32
- McConnell D., et al., 2020, *PASA*, 37, e048
- McCracken H. J., et al., 2012, *A&A*, 544, A156
- Meyer M., 2009, Exploring the HI Universe with ASKAP. eprint: arXiv:0912.2167, doi:10.22323/1.089.0015
- Mohan N., Rafferty D., 2015, *Astrophys. Source Code Libr.*, p. ascl:1502.007
- Murphy E. J., et al., 2011, *ApJ*, 737, 67
- Murphy E. J., et al., 2012, *ApJ*, 761, 97
- Niklas S., Klein U., Wielebinski R., 1997, *A&A*, 322, 19
- Noll S., Burgarella D., Giovannoli E., Buat V., Marcellac D., Muñoz-Mateos J. C., 2009, *A & A*, 507, 1793
- Norris R. P., et al., 2011, *PASA*, 28, 215
- Norris R. P., et al., 2022, *MNRAS*, 513, 1300
- Oesch P. A., et al., 2016, *ApJ*, 819, 129
- Offringa A. R., et al., 2014, *MNRAS*, 444, 606
- Oliver S. J., et al., 2012, *MNRAS*, 424, 1614
- Planck Collaboration et al., 2016, *A&A*, 594, A13
- Price R., Duric N., 1992, *ApJ*, 401, 81
- R Core Team 2020, R: A Language and Environment for Statistical Computing, R Foundation for Statistical Computing
- Robotham A. S. G., 2016a, *Astrophysics Source Code Library*, p. ascl:1602.011
- Robotham A. S. G., 2016b, *Astrophysics Source Code Library*, p. ascl:1604.004
- Robotham A. S. G., Obreschkow D., 2015, *PASA*, 32, e033
- Robotham A. S. G., Davies L. J. M., Driver S. P., Koushan S., Taranu D. S., Casura S., Liske J., 2018, *MNRAS*, 476, 3137
- Robotham A. S. G., Bellstedt S., Lagos C. d. P., Thorne J. E., Davies L. J., Driver S. P., Bravo M., 2020, *MNRAS*, 495, 905
- Salpeter E. E., 1955, *ApJ*, 121, 161
- Sanders D. B., et al., 2007, *ApJS*, 172, 86
- Schinnerer E., et al., 2007, *ApJS*, 172, 46
- Seymour N., et al., 2020, *PASA*, 37, e013
- Seymour N., et al., 2022, *PASA*, 39, e016
- Shimwell T. W., et al., 2022, *A&A*, 659, A1
- Silva L., Granato G. L., Bressan A., Danese L., 1998, *ApJ*, 509, 103
- Smith D. J. B., et al., 2021, *A&A*, 648, A6
- Smolčić V., et al., 2017, *A&A*, 602, A2
- Tabatabaei F. S., et al., 2017, *ApJ*, 836, 185
- Taylor E. N., et al., 2011, *MNRAS*, 418, 1587
- Thorne J. E., et al., 2021, *MNRAS*, 505, 540
- Thorne J. E., et al., 2022a, *MNRAS*, 509, 4940
- Thorne J. E., et al., 2022b, *MNRAS*, 517, 6035
- Walcher C. J., Groves B., Budavari T., Dale D., 2011, *Ap&SS*, 331, 1
- Whittam I. H., et al., 2022, *MNRAS*
- Wright E. L., et al., 2010, *AJ*, 140, 1868
- Zamojski M. A., et al., 2007, *ApJSS*, 172, 468
- Zibetti S., Charlot S., Rix H.-W., 2009, *MNRAS*, 400, 1181
- da Cunha E., et al., 2015, *ApJ*, 806, 110
- de Gasperin F., et al., 2023, The LOFAR LBA Sky Survey II. First Data Release, doi:10.48550/arXiv.2301.12724
- van der Vlugt D., et al., 2021, *ApJ*, 907, 5

APPENDIX A: FITS TO THE KINGFISHER GALAXY SAMPLE

This Appendix presents the ProSPECT fits to the sample of 24 KINGFISHER galaxies as described in Section 3. The physical quantities for each of the galaxies are given in Table A1 and provided as supplementary material. Figure A1 shows the resulting SED fit, star formation and metallicity history for an example galaxy (NGC 4826) where equivalent figures for the rest of the KINGFISHER sample are available as supplementary material.

APPENDIX B: COMPARISON OF DERIVED KINGFISH GALAXY PROPERTIES

The SEDs of the 61 KINGFISH galaxies were previously fit by Hunt et al. (2019) using the FUV-sub millimeter (850 μm) photometry presented in Dale et al. (2017). The fitting was performed using CIGALE (Noll et al. 2009; Boquien et al. 2019), MAGPHYS (Da Cunha et al. 2008), and GRASIL (Silva et al. 1998) each adopting the Bruzual & Charlot (2003) SSPs with a Chabrier (2003) IMF. For more details about the specific implementations of each model, see Hunt et al. (2019) however we briefly describe each method below.

In the cases of CIGALE and MAGPHYS, simple parameteric SFHs are used with an exponential plus burst parameterisation for MAGPHYS and a delayed exponential with truncation used for CIGALE. For GRASIL, the SFR at any given time is proportional to the available gas mass where the star formation efficiency and exponential folding timescale of the infalling gas are modelled as free parameters. When fitting with CIGALE, a constant $Z = 0.02$ metallicity is adopted while MAGPHYS assumes a constant metallicity but the value of which is fit as a free

Table A1. Parameters derived by ProSPECT for the sample of KINGFISHER galaxies. Full table available online.

Galaxy	$\log_{10} \left(\frac{M_{\star}}{M_{\odot}} \right)$	$\log_{10} \left(\frac{\text{SFR}}{M_{\odot} \text{yr}^{-1}} \right)$	$\log_{10} \left(\frac{M_{\text{dust}}}{M_{\odot}} \right)$	$\log_{10} \left(\frac{L_{\text{dust}}}{L_{\odot}} \right)$	$\log_{10} (f_{\text{IR}})$	α_{sy}
IC2574	8.53 ^{+0.09} _{-0.25}	-1.17 ^{+0.08} _{-0.12}	5.97 ^{+0.18} _{-0.18}	8.29 ^{+0.07} _{-0.08}	-0.83 ^{+0.33} _{-0.43}	-0.49 ^{+0.49} _{-1.09}
NGC 0337	9.60 ^{+0.12} _{-0.07}	0.02 ^{+0.09} _{-0.30}	7.56 ^{+0.15} _{-0.14}	10.01 ^{+0.07} _{-0.09}	-1.28 ^{+0.35} _{-0.20}	-1.30 ^{+0.54} _{-0.36}
NGC 0628	10.01 ^{+0.09} _{-0.13}	-0.24 ^{+0.21} _{-0.11}	7.57 ^{+0.27} _{-0.04}	9.86 ^{+0.05} _{-0.08}	-0.88 ^{+0.27} _{-0.14}	-1.02 ^{+0.52} _{-0.43}
NGC 1266	10.59 ^{+0.08} _{-0.08}	-1.30 ^{+0.48} _{-20.02}	7.29 ^{+0.14} _{-0.87}	10.23 ^{+0.08} _{-0.20}	-1.39 ^{+0.26} _{-0.30}	-1.05 ^{+0.40} _{-0.36}
NGC 1482	10.49 ^{+0.07} _{-0.09}	-0.17 ^{+0.28} _{-0.76}	7.66 ^{+0.19} _{-0.11}	10.63 ^{+0.06} _{-0.06}	-1.08 ^{+0.23} _{-0.26}	-1.20 ^{+0.39} _{-0.38}
NGC 2146	10.96 ^{+0.07} _{-0.13}	0.56 ^{+0.35} _{-0.05}	7.92 ^{+0.31} _{-0.18}	11.04 ^{+0.11} _{-0.08}	-1.11 ^{+0.18} _{-0.12}	-0.87 ^{+0.17} _{-0.25}
NGC 2798	10.33 ^{+0.04} _{-0.13}	0.29 ^{+0.12} _{-0.09}	7.39 ^{+0.20} _{-0.15}	10.54 ^{+0.03} _{-0.09}	-0.75 ^{+0.19} _{-0.37}	-0.82 ^{+0.48} _{-0.60}
NGC 2841	11.11 ^{+0.06} _{-0.05}	-26.10 ^{+20.02} _{-55.75}	8.05 ^{+0.07} _{-0.16}	10.00 ^{+0.05} _{-0.06}	-1.11 ^{+0.32} _{-0.19}	-1.01 ^{+0.83} _{-0.74}
NGC 2976	9.26 ^{+0.12} _{-0.04}	-1.31 ^{+0.19} _{-0.30}	6.59 ^{+0.15} _{-0.21}	8.87 ^{+0.05} _{-0.08}	-1.04 ^{+0.49} _{-0.23}	-1.07 ^{+0.68} _{-0.83}
NGC 3049	9.50 ^{+0.04} _{-0.14}	-0.48 ^{+0.12} _{-0.12}	7.14 ^{+0.13} _{-0.30}	9.54 ^{+0.05} _{-0.08}	-0.79 ^{+0.29} _{-0.27}	-1.13 ^{+1.13} _{-1.07}
NGC 3077	9.65 ^{+0.04} _{-0.21}	-23.08 ^{+21.27} _{-11.98}	6.26 ^{+0.13} _{-0.15}	8.84 ^{+0.04} _{-0.07}	-0.50 ^{+0.00} _{-0.22}	-0.54 ^{+0.54} _{-0.85}
NGC 3184	10.14 ^{+0.06} _{-0.09}	0.14 ^{+0.06} _{-0.07}	7.77 ^{+0.19} _{-0.12}	9.95 ^{+0.04} _{-0.07}	-0.83 ^{+0.15} _{-0.12}	-1.00 ^{+0.46} _{-1.20}
NGC 3190	10.86 ^{+0.03} _{-0.09}	-151.19 ^{+132.72} _{-inf}	7.56 ^{+0.12} _{-0.10}	9.75 ^{+0.07} _{-0.05}	-1.13 ^{+0.31} _{-0.24}	-0.93 ^{+0.57} _{-0.71}
NGC 3265	9.48 ^{+0.03} _{-0.07}	-0.90 ^{+0.19} _{-0.08}	6.47 ^{+0.29} _{-0.15}	9.37 ^{+0.08} _{-0.08}	-1.05 ^{+0.55} _{-0.18}	-1.02 ^{+1.02} _{-0.52}
NGC 3627	10.68 ^{+0.09} _{-0.07}	-0.04 ^{+0.16} _{-0.58}	7.86 ^{+0.22} _{-0.08}	10.38 ^{+0.05} _{-0.08}	-1.09 ^{+0.48} _{-0.08}	-1.28 ^{+0.99} _{-0.48}
NGC 3938	10.30 ^{+0.10} _{-0.07}	0.41 ^{+0.05} _{-0.15}	7.93 ^{+0.14} _{-0.10}	10.20 ^{+0.04} _{-0.05}	-0.93 ^{+0.35} _{-0.20}	-1.08 ^{+0.72} _{-1.00}
NGC 4236	9.01 ^{+0.21} _{-0.08}	-0.92 ^{+0.13} _{-0.56}	6.31 ^{+0.29} _{-0.30}	8.65 ^{+0.07} _{-0.12}	-1.02 ^{+0.52} _{-0.56}	-0.98 ^{+0.82} _{-0.94}
NGC 4254	10.42 ^{+0.03} _{-0.26}	0.53 ^{+0.15} _{-0.06}	8.17 ^{+0.12} _{-0.13}	10.56 ^{+0.04} _{-0.08}	-1.12 ^{+0.14} _{-0.17}	-0.94 ^{+0.25} _{-0.39}
NGC 4321	10.66 ^{+0.04} _{-0.07}	0.49 ^{+0.09} _{-0.12}	8.10 ^{+0.28} _{-0.10}	10.47 ^{+0.06} _{-0.08}	-1.03 ^{+0.49} _{-0.27}	-1.02 ^{+0.88} _{-0.50}
NGC 4536	10.35 ^{+0.07} _{-0.17}	0.23 ^{+0.15} _{-0.09}	7.72 ^{+0.29} _{-0.13}	10.31 ^{+0.04} _{-0.08}	-0.97 ^{+0.26} _{-0.24}	-1.01 ^{+0.40} _{-0.39}
NGC 4559	9.49 ^{+0.12} _{-0.10}	-0.35 ^{+0.12} _{-0.05}	7.19 ^{+0.14} _{-0.16}	9.42 ^{+0.06} _{-0.06}	-1.00 ^{+0.13} _{-0.14}	-0.98 ^{+0.40} _{-1.22}
NGC 4569	10.41 ^{+0.03} _{-0.10}	-0.83 ^{+0.39} _{-0.22}	7.42 ^{+0.21} _{-0.11}	9.67 ^{+0.05} _{-0.07}	-1.23 ^{+0.17} _{-0.24}	-0.83 ^{+0.25} _{-1.37}
NGC 4579	10.95 ^{+0.08} _{-0.04}	-0.31 ^{+0.10} _{-0.63}	7.84 ^{+0.12} _{-0.15}	9.98 ^{+0.06} _{-0.06}	-1.42 ^{+0.40} _{-0.16}	-0.46 ^{+0.46} _{-0.37}
NGC 4594	11.13 ^{+0.06} _{-0.03}	-4.70 ^{+2.94} _{-14.62}	7.52 ^{+0.10} _{-0.12}	9.49 ^{+0.06} _{-0.06}	-1.37 ^{+0.17} _{-0.28}	0.00 ^{+0.00} _{-0.40}
NGC 4631	9.89 ^{+0.20} _{-0.16}	0.38 ^{+0.05} _{-0.11}	7.90 ^{+0.15} _{-0.16}	10.30 ^{+0.05} _{-0.07}	-1.18 ^{+0.20} _{-0.16}	-0.78 ^{+0.33} _{-0.25}
NGC 4725	10.81 ^{+0.03} _{-0.15}	-0.27 ^{+0.30} _{-0.25}	7.84 ^{+0.10} _{-0.11}	9.82 ^{+0.05} _{-0.07}	-1.13 ^{+0.17} _{-0.16}	-1.03 ^{+0.29} _{-0.39}
NGC 4736	10.34 ^{+0.07} _{-0.02}	-0.42 ^{+0.08} _{-0.42}	7.08 ^{+0.20} _{-0.08}	9.73 ^{+0.04} _{-0.13}	-0.73 ^{+0.10} _{-0.22}	-0.98 ^{+0.53} _{-0.59}
NGC 4826	10.29 ^{+0.10} _{-0.06}	-1.03 ^{+0.24} _{-0.39}	7.05 ^{+0.12} _{-0.12}	9.49 ^{+0.06} _{-0.08}	-0.71 ^{+0.21} _{-0.19}	-0.89 ^{+0.49} _{-0.95}
NGC 5055	10.75 ^{+0.03} _{-0.09}	-0.01 ^{+0.19} _{-0.18}	7.99 ^{+0.24} _{-0.10}	10.27 ^{+0.04} _{-0.11}	-0.90 ^{+0.08} _{-0.21}	-1.25 ^{+0.63} _{-0.33}
NGC 5457	10.34 ^{+0.04} _{-0.10}	0.50 ^{+0.07} _{-0.10}	8.03 ^{+0.16} _{-0.15}	10.28 ^{+0.06} _{-0.06}	-0.93 ^{+0.18} _{-0.20}	-0.73 ^{+0.35} _{-0.73}
NGC 5713	10.46 ^{+0.10} _{-0.08}	0.26 ^{+0.08} _{-0.26}	7.74 ^{+0.18} _{-0.11}	10.48 ^{+0.03} _{-0.07}	-0.96 ^{+0.15} _{-0.24}	-0.97 ^{+0.42} _{-0.36}
NGC 5866	10.63 ^{+0.13} _{-0.10}	-1.90 ^{+0.67} _{-7.43}	7.35 ^{+0.15} _{-0.18}	9.43 ^{+0.12} _{-0.11}	-1.16 ^{+0.54} _{-0.66}	-0.65 ^{+0.65} _{-1.25}
NGC 6946	10.64 ^{+0.11} _{-0.13}	0.25 ^{+0.30} _{-0.11}	8.05 ^{+0.18} _{-0.11}	10.50 ^{+0.06} _{-0.05}	-0.96 ^{+0.38} _{-0.32}	-0.67 ^{+0.60} _{-0.56}
NGC 7331	11.03 ^{+0.01} _{-0.15}	0.26 ^{+0.23} _{-0.16}	8.32 ^{+0.16} _{-0.11}	10.64 ^{+0.05} _{-0.07}	-1.12 ^{+0.27} _{-0.17}	-1.32 ^{+0.45} _{-0.41}

parameter. As GRASIL models the chemical evolution of galaxies, the metallicity of a galaxy within the model evolves over time and is modelled by a free parameter. To model the attenuation by dust MAGPHYS adopts the two-component model from Charlot & Fall (2000) while CIGALE uses a modified star burst attenuation law (e.g. Calzetti et al. 2000) with differing redenning for stellar populations of different ages (essentially the same assumption as the two-component Charlot & Fall 2000 model). GRASIL uses geometry-dependent radiative transfer assuming the Laor & Draine (1993) grain opacities to model both the effects of attenuation and emission by dust. Re-emission by dust in the FIR is assumed to follow energy-balance in both MAGPHYS and CIGALE however CIGALE uses the dust models of Draine et al. (2007, 2014) while MAGPHYS assumes a modified grey-body.

Figure B1 shows comparisons of the stellar masses, SFRs, dust masses, and dust luminosities as derived by Hunt et al. (2019) to

those presented in this work. For each parameter, we compare to the properties as derived by MAGPHYS (black), CIGALE (red), and GRASIL (blue). We find that ProSPECT recovers systematically higher stellar masses when compared to MAGPHYS, CIGALE, and GRASIL. As discussed in Thorne et al. (2021) this is predominantly the result of a more flexible SFH implementation but also the inclusion of an evolving metallicity history. We also find that the use of a more flexible SFH results in systematically lower SFRs, especially when compared to GRASIL. The recovered dust luminosities are in good agreement, however, this does not translate to a good agreement in the dust masses due to different assumptions of the mass-to-light ratio which is highlighted by the clear offsets between SED fitting codes. The mass-to-light ratio assumed by GRASIL results in systematically larger dust masses than MAGPHYS, CIGALE, or ProSPECT.

This paper has been typeset from a \LaTeX file prepared by the author.

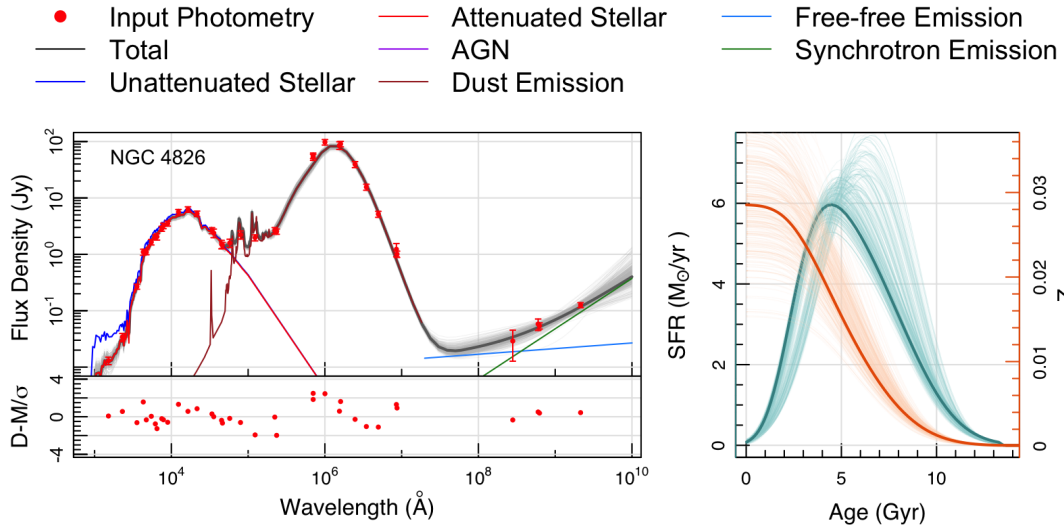


Figure A1. Example of FUV-radio SED fit to NGC 4826 from the KINGFISHER sample based on the measurements from Dale et al. (2017) and Tabatabaei et al. (2017) (red) overlaid with the best fitting PROSPECT total SED (black), stellar unobscured (blue) and obscured (red), dust (brown), radio synchrotron (green) and free-free (light blue) emission. The sampling of the final MCMC posterior is shown in (grey) to illustrate the uncertainty in the fits. The lower left panel shows the residuals for each measurement (data - model / error). The right panel shows the best-fit SFH (green) and metallicity history (orange) along with the sampling of the posterior for both histories (lighter shades). Equivalent figures for the rest of the sample are made available as supplementary material.

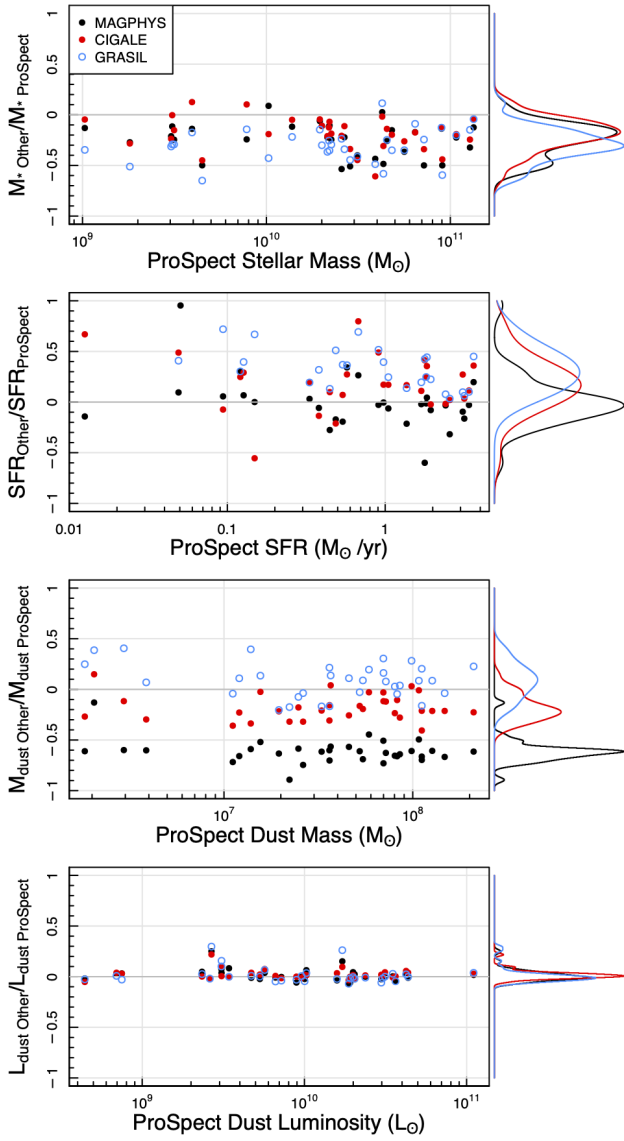


Figure B1. Comparisons of stellar mass, SFR, dust mass, and dust luminosity derived using ProSPECT for the KINGFISH sample to those presented in [Hunt et al. \(2019\)](#) using GRASIL (blue), CIGALE (red), and MAGPHYS (black). The right panel shows the projected density for each comparison.